An Airborne Study of an Atmospheric River over the Subtropical Pacific during WISPAR: Dropsonde Budget-Box Diagnostics and Precipitation Impacts in Hawaii

PAUL J. NEIMAN AND GARY A. WICK

Physical Sciences Division, NOAA/Earth System Research Laboratory, Boulder, Colorado

BENJAMIN J. MOORE

Cooperative Institute for Research in the Environmental Sciences, NOAA/Earth System Research Laboratory, Boulder, Colorado and Department of Atmospheric and Environmental Sciences, University at Albany, State University of New York, Albany, New York

F. MARTIN RALPH

Scripps Institution of Oceanography, La Jolla, California

J. RYAN SPACKMAN

Science and Technology Corporation, NOAA/Earth System Research Laboratory, Boulder, Colorado

BILL WARD

NOAA/NWS/Pacific Region Headquarters, Honolulu, Hawaii

(Manuscript received 29 November 2013, in final form 13 March 2014)

ABSTRACT

The Winter Storms and Pacific Atmospheric Rivers (WISPAR) experiment was carried out in January–March 2011 from the National Aeronautics and Space Administration (NASA) Dryden Flight Research Center as a demonstration for utilizing unmanned aerial systems in meteorological research and operations over data-sparse oceans. One of the campaign's three missions was coordinated with a manned National Oceanic and Atmospheric Administration Gulfstream-IV (G-IV) flight out of Honolulu, Hawaii, on 3–4 March 2011. The G-IV, which flew through a developing atmospheric river (AR) west of Hawaii, represents the cornerstone observing platform for this study and provided the southernmost dropsonde observations of an AR published to date in the subtropical Northern Hemisphere. The AR exhibited characteristics comparable to those observed in previous studies farther north in the subtropics and midlatitudes, save for larger integrated water vapor and weaker winds in the AR core and stronger equatorward vapor fluxes in the shallow post-cold-frontal northeasterly flow. Eight dropsondes released in a ~200-km-wide box formation provided a novel kinematic assessment of tropospheric vorticity, divergence (mass, water vapor, sensible heat), and vertical velocity in the AR region, as well as sea surface fluxes. The budget-box diagnostics were physically consistent with global-gridded reanalysis datasets, while also providing useful additional kinematic and thermodynamic information on the mesoscale. Meteorological impacts of the AR were assessed on Hawaii's island of Kauai, where the state's heaviest rainfall was observed for this case. Rainfall on Kauai was modulated significantly by its steep orography, including on the normally dry side of the island where heavy rains fell.

1. Introduction

Atmospheric rivers (ARs) are critical to study and monitor because of their potential for bringing extreme precipitation to nearshore and inland regions upon landfall. ARs, as termed originally by Zhu and Newell (1994, 1998), are narrow filaments of enhanced water vapor transport within the lower troposphere (≤~3 km MSL) in the warm sector of some extratropical cyclones (Neiman et al. 2008a). Numerous studies have documented important hydrological impacts of ARs in multiple midlatitude regions. For example, ARs have been

Corresponding author address: Paul J. Neiman, Physical Sciences Division, NOAA/Earth System Research Laboratory, Mail Code R/PSD2, 325 Broadway, Boulder, CO 80305.
E-mail: paul.j.neiman@noaa.gov

DOI: 10.1175/MWR-D-13-00383.1

linked to flooding in California (Ralph et al. 2006), the Pacific Northwest (Neiman et al. 2008b, 2011), Arizona (Neiman et al. 2013), the central United States (Moore et al. 2012), western South America (Viale and Nuñez 2011; Garreaud 2013), western Europe (Lavers et al. 2011; Lavers and Villarini 2013), and Norway (Stohl et al. 2008; Sodemann and Stohl 2013), as well as extreme snowfall in the Sierra Nevada (Guan et al. 2010, 2013). Landfalling storms with AR attributes have even been known to generate extreme precipitation in subtropical northwestern Africa (e.g., Knippertz and Martin 2005). ARs also yield important benefits because they provide essential seasonal water supply (e.g., Dettinger et al. 2011).

While the majority of these studies relied on ground-based, satellite, or reanalysis data, much of our observational understanding of ARs has been derived from aircraft observations. Ralph et al. (2004) analyzed dropsonde data from a National Oceanic and Atmospheric Administration (NOAA) P-3 aircraft of an AR offshore of California in January 1998 to characterize the vertical cross section across that AR. These measurements demonstrated that the water vapor flux (resulting from the combination of strong winds and large water vapor content) in an AR is focused at low altitude in a narrow region ahead of a cold front. The observations also guided the use of satellite-derived integrated water vapor (IWV) data as a proxy for the identification of ARs as employed in many of the previously cited papers. Additional analysis of dropsonde data from 17 storms sampled from the NOAA P-3 in 1998 and 2001 (Ralph et al. 2005) characterized the mean vertical profiles of wind speed, water vapor, and water vapor transport, thus confirming the shallow characteristic height of transport in ARs (75% of the transport occurred below 2.25-km altitude) and illustrating the typical AR strength in midlatitudes upstream of orographic influence. In 2005, a NOAA P-3 based in Hawaii provided initial direct observations of water vapor transport near the interface between the tropics and subtropics to address whether ARs can effectively ''tap'' into and transport tropical moisture. Though just one case, the observations documented northward advection of tropical water vapor into the subtropical extension of a midlatitude AR (Ralph et al. 2011).

Despite these efforts, critical knowledge gaps remain regarding the structure, evolution, and hydrometeorological influences of ARs, especially in subtropical regions. Of particular interest is deriving a water vapor budget in ARs to determine the source and evolution of water within them. While Ralph et al. (2011) did observe the transport of tropical water vapor into the subtropics, the data did not demonstrate how far into the midlatitudes the water was carried as opposed to possible rainout along the way. The relative roles of long-range water vapor transport and convergence within ARs have been studied by Bao et al. (2006), Stohl et al. (2008), and Cordeira et al. (2013), but only using model-based data. Cordeira et al. (2013) considered model-based changes in IWV resulting from precipitation. The representation of water vapor transport and precipitation in model-based datasets, however, has not been comprehensively validated. Satellite retrievals only partially guide model analyses and are unable to fully address the water budget because the limited wind profile retrievals at low levels and the coarse vertical resolution of water vapor retrievals preclude accurate measurements of water vapor transport. Given these limited observational inputs available to the models over the oceans, it is important to conduct research using direct observations to gain further insight into the water budget and corroborate model-derived findings. Last, the impact of ARs in subtropical regions such as Hawaii is not well documented, and it is unclear if they have the same potential connection to extreme precipitation in those regions as in the midlatitudes.

The NOAA-led Winter Storms and Pacific Atmospheric Rivers (WISPAR) experiment was conducted, in part, as a first step to explore these critical gaps in our understanding of ARs. WISPAR was funded by NOAA's Unmanned Aircraft Systems program in partnership with the National Aeronautics and Space Administration (NASA), with the primary goal of assessing the capability of the NASA Global Hawk (GH) unmanned aircraft and its dropsonde system to support NOAA research and operational applications associated with high impact weather over the Pacific and Arctic. The experiment was conducted in January through March 2011, based out of NASA's Dryden Flight Research Center (DFRC) at Edwards Air Force Base in California. As part of a research focus on observing AR structure and evolution, one of three GH flights was coordinated with a NOAA Gulfstream-IV (G-IV) Winter Storms Reconnaissance Program flight from Honolulu, Hawaii, on 3–4 March 2011, to which a dedicated AR cross section and kinematic budget box were added in support of WISPAR.

The G-IV aircraft sampled the AR, whose evolution over 4 days is captured by the satellite-derived IWV imagery in Fig. 1. The AR, which exhibited a potential connection to tropical moisture, directly impacted the Hawaiian island of Kauai and later extended to the West Coast of the continental United States. The G-IV flight was especially revealing in that it 1) yielded the southernmost airborne AR observations to date in the subtropical Northern Hemisphere, 2) provided a novel dropsonde-based mesoscale kinematic budget-box

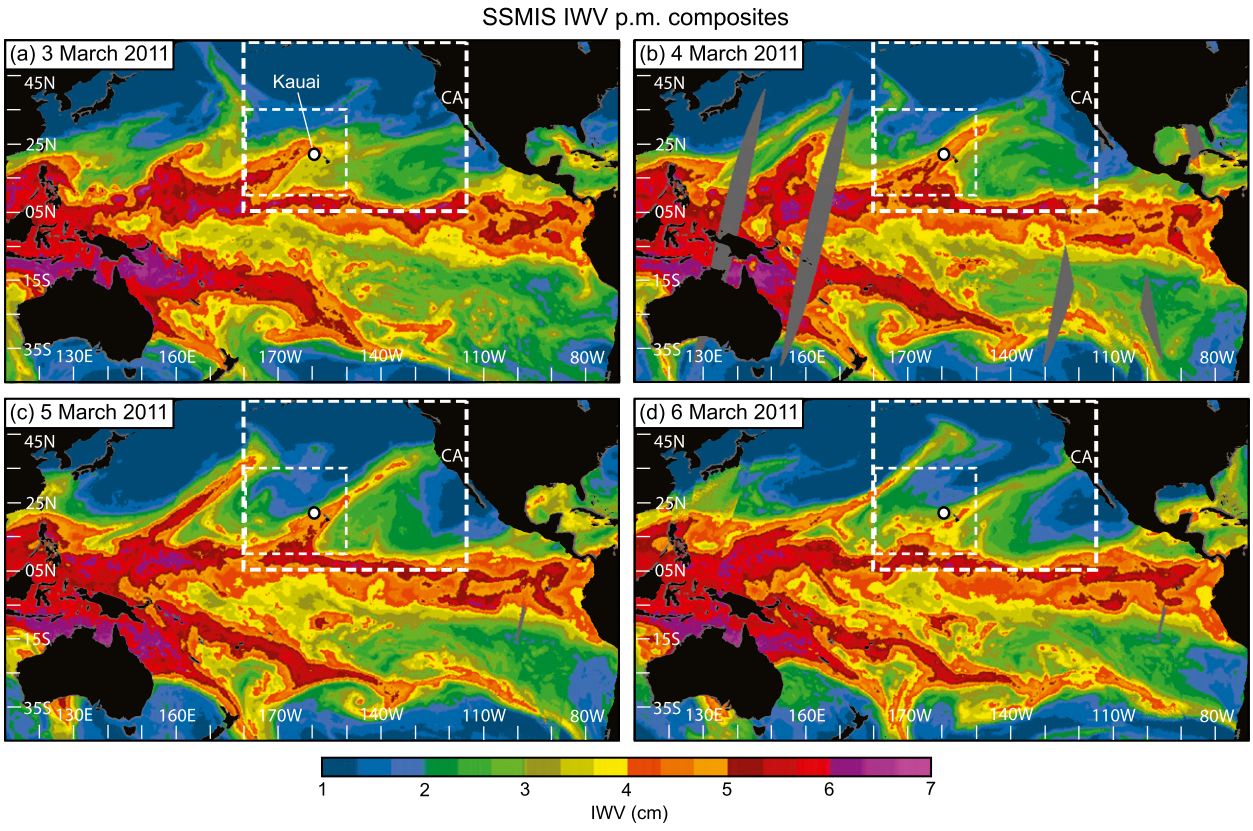

FIG. 1. Composite Pacific basin SSMIS satellite imagery of IWV (cm; color scale at bottom) constructed from polar-orbiting swaths between 1200 and 2359 UTC (a) 3, (b) 4, (c) 5, and (d) 6 Mar 2011. The island of Kauai, HI, is marked. The outer white box shows the domain of the CFSR analyses in Figs. 2–5, and the inner white box marks the domain of the SSMIS and aircraft analyses in Figs. 8–10.

diagnostic within an AR through the depth of the troposphere, and 3) occurred in close proximity to the Hawaiian islands, allowing for a first-of-its-kind assessment of key AR impacts on the islands. This paper addresses each of these themes through analysis of the dropsonde data in concert with satellite-derived observations, reanalysis datasets, and available ground-based measurements.

2. Observing systems and gridded datasets

The cornerstone observing platform for this study is the NOAA G-IV twin-jet aircraft (www.aoc.noaa.gov/aircraft_g4.htm). It has a cruising altitude of ~13.5 km MSL, a cruising speed of ~230 m s^{-1}, a maximum range of ~7000 km (~8.75-h duration), and 8 dropsonde channels. The dropsondes use the GPS-based Airborne Vertical Atmospheric Profiling System (www.eol.ucar.edu/isf/facilities/dropsonde) to obtain profiles of barometric pressure (±1 hPa), wind velocity (±0.5 m s^{-1}), temperature (±0.2°C), and relative humidity (±5%) with high vertical resolution (i.e., measurements are taken every 0.5 s for the thermodynamic variables and 0.25 s for winds, corresponding to approximately 6- and 3-m resolution, respectively, near the surface). The WISPAR G-IV flight was based out of Honolulu, Hawaii, and was carried out between 1934 UTC 3 March and 0326 UTC 4 March 2011 (e.g., Fig. 8) in coordination with the Winter Storms Reconnaissance Program (e.g., Szunyogh et al. 2002). A total of 42 dropsondes successfully gathered data during this flight.

Satellite-based retrievals of IWV, cloud liquid water (CLW), and rain rate (RR) were obtained from the Special Sensor Microwave Imager/Sounder (i.e., SSMIS; Kunkee et al. 2008) on board three polar-orbiting satellites (*F16*, *F17*, and *F18*) that circled the globe every ~102 min. The retrievals, which have a native resolution of ~40 km in ~1400-km-wide swaths, were placed on a ~25-km-resolution grid and combined into twice-daily composite images corresponding to the time intervals between 0000 and 1159 UTC (a.m. composites) and 1200 and 2359 UTC (p.m. composites). The IWV was retrieved using the Wentz (1995) optimal statistical algorithm, whereas the CLW and RR retrievals are described in Karstens et al. (1994) and Berg and Chase (1992), respectively.

Two global gridded datasets from NOAA's National Centers for Environmental Prediction (NCEP) provided synoptic-scale context: 1) the Climate Forecast System Reanalysis (CFSR), used for plan-view analyses; and 2) the CFSR-based Global Data Assimilation System (GDAS), used for trajectory analyses. The CFSR analyses (Saha et al. 2010) are available every 6 h at 0.5° × 0.5° horizontal resolution with 37 levels starting in 1979. The GDAS analyses are available every 6 h with 1.0° × 1.0° horizontal resolution; the vertical resolution is 25 hPa between 1000 and 900 hPa and 50 hPa aloft. Backward and forward air parcel trajectories were computed from the GDAS analyses using the Hybrid Single-Particle Lagrangian Integrated Trajectory (HYSPLIT) model (Draxler and Hess 1997; Draxler and Rolph 2011).

To quantify the landfalling impacts of the AR on Hawaii, additional datasets were utilized. Namely, twice-daily operational rawinsondes from Lihue (LIH) and Hilo (ITO) were analyzed. Also, automated rain gauges provided 3-h rainfall accumulations across the state, including in difficult-to-reach locales.

3. Reanalysis-based synoptic overview

This section provides a model-based synoptic overview of the AR and its environs. The vertically integrated 1000–300-hPa horizontal water vapor transport [IVT; see Neiman et al. (2008a) for calculation method] is shown in Fig. 2 at 24-h intervals between 0000 UTC 4 and 7 March, corresponding roughly to the times of the SSMIS IWV satellite imagery in Fig. 1. The analyses portray the development of a northeastward-directed IVT plume exceeding 200–300 kg s^{-1} m^{-1} associated with the AR near Hawaii at 0000 UTC 4 and 5 March 2011 (Figs. 2a,b). This period was characterized by the poleward entrainment of tropical water vapor into the AR. By 0000 UTC 6 March and thereafter (Figs. 2c,d), the tropical connection was severed, and the AR weakened dramatically while making landfall in California. Not surprisingly, precipitation along the mountainous U.S. West Coast during the AR landfall was modest [~(25–100) mm; not shown] in comparison to strong landfalling ARs cited earlier.

Companion analyses at 925 hPa, 500 hPa, and the surface are presented in Figs. 3–5. At 0000 UTC 4 March (Fig. 3a), a 925-hPa subtropical trough near the developing AR west of Hawaii produced warm, moist, low-level southerly flow with high equivalent potential temperatures (θ_e). The trough resided beneath a southern branch shortwave trough at 500 hPa (Fig. 4a) and was decoupled from a large 925-hPa extratropical cyclone north of 40°N. An analysis of surface latent heat flux (Fig. 5a) shows water vapor input exceeding 100 W m^{-2} from the ocean surface into the developing AR. The AR is defined in Fig. 5 using a minimum IVT threshold of 250 kg s^{-1} m^{-1}; the rationale for choosing this threshold is provided in section 4a in the context of dropsonde cross-section analyses. By 0000 UTC 5 March (Figs. 3b–5b), the 925-hPa subtropical trough moved northeastward with the 500-hPa shortwave aloft and developed a closed circulation and a plume of warm, moist, high-θ_e air within the AR. Low-level southwesterly flow in the AR impacted southern Hawaii, while the winds shifted to northeasterly within a weak cold-frontal θ_e gradient over the northern part of the state. Upward sea surface latent heat fluxes persisted beneath the AR but areal extent decreased from 24 h earlier. One day later at 0000 UTC 6 March (Figs. 3c–5c), the 925-hPa subtropical trough and its moist baroclinic structure advanced toward the U.S. West Coast, while the corresponding southern branch shortwave at 500 hPa became entrained into the northern branch flow. The 925-hPa θ_e plume ahead of the subtropical trough and within the advancing southwesterly AR airstream lost lower-tropospheric heat and moisture relative to 24 h earlier, consistent with the fact that 1) upward sea surface latent heat fluxes beneath the AR nearly ceased (Fig. 5c), 2) synoptic forcing (e.g., Fig. 4c) and related moisture convergence (not shown) was weak, and 3) tropical water vapor was no longer exported into the AR (Fig. 2c). By 0000 UTC 7 March (Figs. 3d–5d), the 925-hPa subtropical trough dissipated, and the θ_e plume within the landfalling AR weakened further while drifting southward. The shortwave trough at 500 hPa approached California in a consolidated northern branch airstream, and sea surface latent heat fluxes into the weakening AR were minimal.

To further quantify the synoptic conditions in the developing AR near Hawaii, a Lagrangian approach was employed by computing 2 × 4 arrays of HYSPLIT 84-h backward (forward) air parcel trajectories ending (beginning) at 0000 UTC 4 March 2011 at 1 and 5 km MSL (Figs. 6 and 7); the time corresponds to the middle of the nearby G-IV flight. The southern array (18°–20°N, 168°–162°W; red) is situated in the developing AR and the northern array (26°–28°N, 168°–162°W; blue) is located in the cold-frontal baroclinic zone (Figs. 2a–5a). The backward trajectories at these two arrays (Fig. 6a) show different behaviors: the southern trajectories originated from the tropics whereas their northern counterparts did not. Cluster averaging of the trajectories based on location and final altitude (Figs. 6b–d) also reveal important differences. The southern low-level cluster exhibited weak subsidence and substantial moistening, consistent with upward sea surface latent heat fluxes. In contrast, the southern upper-level cluster experienced modest ascent, absolute drying, and relative moistening, although relative humidity (RH) values <65% preclude

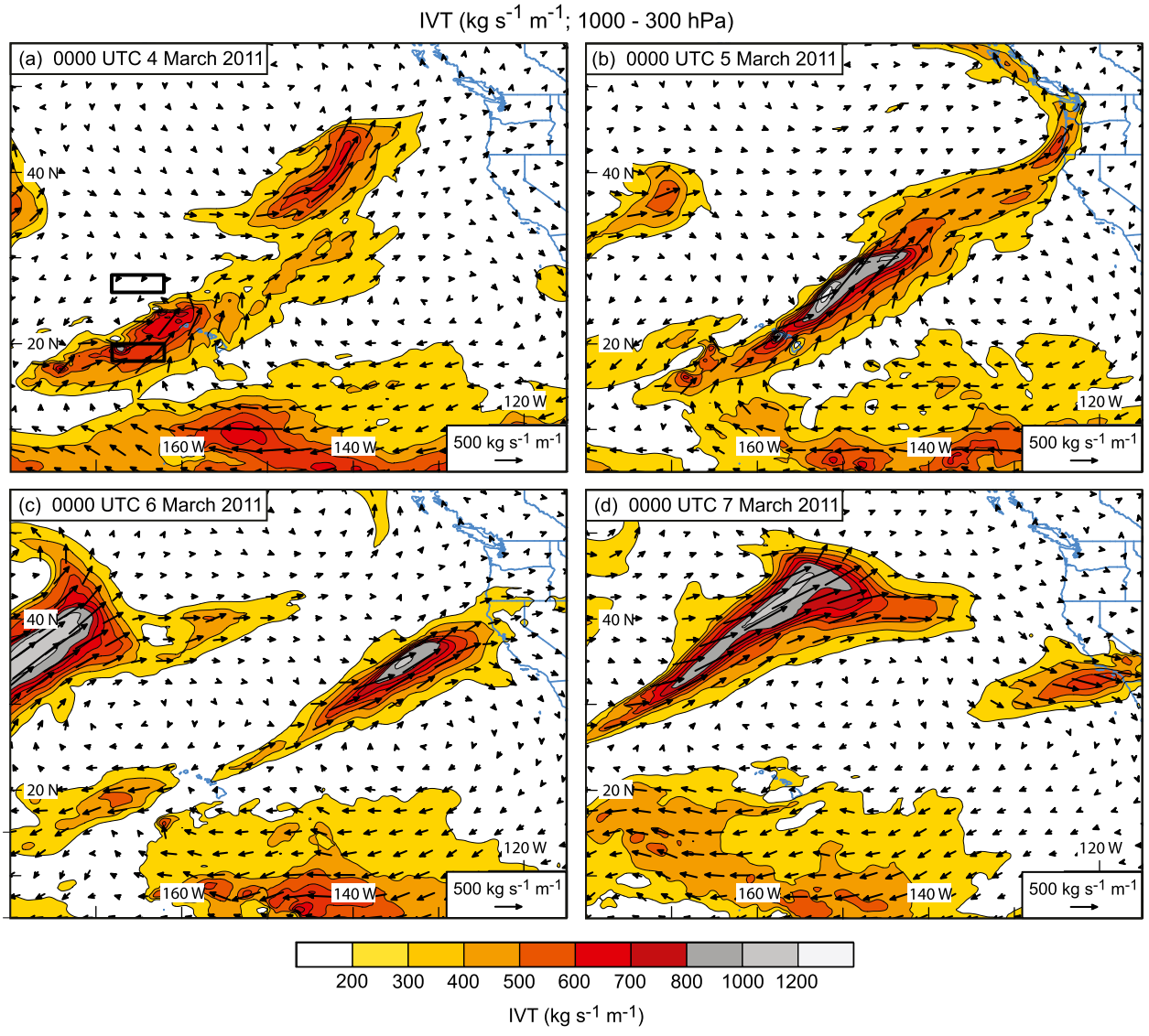

FIG. 2. Plan-view analyses of the 1000–300-hPa IVT (kg s^{-1} m^{-1}; magnitude color scale and vector scale at bottom) from the 0.5° × 0.5° resolution CFSR dataset at 0000 UTC (a) 4, (b) 5, (c) 6, and (d) 7 Mar 2011. The black rectangles in (a) mark the domains of the trajectory arrays in Figs. 6 and 7. Every fifth IVT vector was plotted in longitude, and every fourth in latitude.

rainout. The northern, low-level cluster mirrored the characteristics of the southern low-level cluster, again consistent with upward sea surface latent heat fluxes. The northern upper-level trajectories were subdivided into eastern and western clusters, given their disparate behaviors. The western cluster was subsident and very dry due to its upper-tropospheric midlatitude origin, whereas the eastern cluster experienced strong ascent, relative moistening with RH > 80%, and absolute drying in the final 1–2 days, which is suggestive of substantial rainout.

The forward trajectories starting at these same arrays and time are shown in Fig. 7a. In the southern array, which originated in the AR, all trajectories moved quickly northeastward toward the U.S. West Coast. In contrast, the low-level parcels in the northern array moved southwestward behind the cold front, while their upper-level counterparts drifted mostly southeastward behind the southern branch shortwave trough aloft. The southern lower and upper cluster averages (Figs. 7b–d) reveal strong ascent, relative moistening with RH > 80%, and absolute drying in the first 24–36 h when substantial rainout likely occurred. Thereafter, the parcels subsided but remained high (above 500 hPa) and dry as they crossed the coast. The northern lower cluster exhibited modest parcel ascent, relative moistening, and

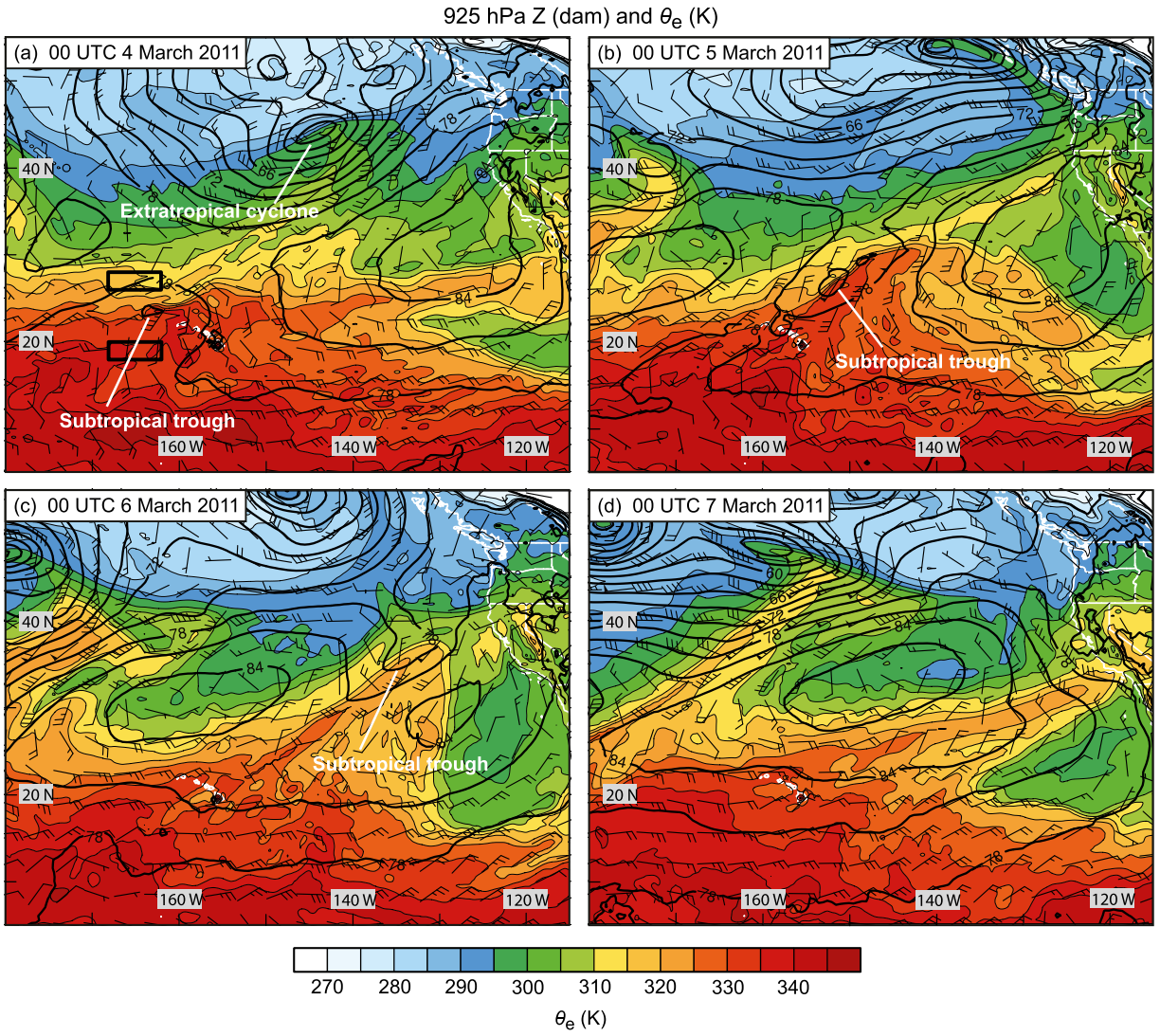

FIG. 3. As in Fig. 2, but for 925-hPa geopotential height (dam; black contours), θ_e (K; color scale at bottom), and wind velocities (flags = 25, barbs = 5, and half barbs = 2.5 m s^{-1}).

absolute drying during the final ~15 h, while the cluster aloft subsided and moistened.

4. Mesoscale dropsonde analysis through the AR

a. *Plan-view and cross-section perspectives*

A total of 44 dropsondes were released from the G-IV near Hawaii between 2007 UTC 3 March and 0302 UTC 4 March 2011. Of those, 42 recorded data successfully in the lower stratosphere and through the troposphere. The G-IV flight track and dropsondes are overlaid on the SSMIS IWV swath at 1921 UTC 3 March 2011 (Fig. 8) to highlight the fact that the southwest–northeast-oriented AR plume was the meteorological target. This image is shown because it is closest in time to the earlier part of the G-IV flight while also providing complete SSMIS coverage over the flight domain. A sea surface temperature analysis is also shown.

To more precisely map the flight track onto the IWV image, the motion of the AR was taken into account by performing a time-to-space adjustment on the flight track (this analysis technique was first applied by Fujita 1963) by invoking Taylor's (1938) hypothesis (i.e., steady-state weather systems propagate at a fixed phase velocity). Sequential IWV images (not shown) reveal that the AR plume drifted southeastward (i.e., from 313°) at 6.5 m s^{-1}, while the leading nose of the AR moved northeastward. The first 14 G-IV dropsondes between 2007 and 2144 UTC 3 March were not time-to-space

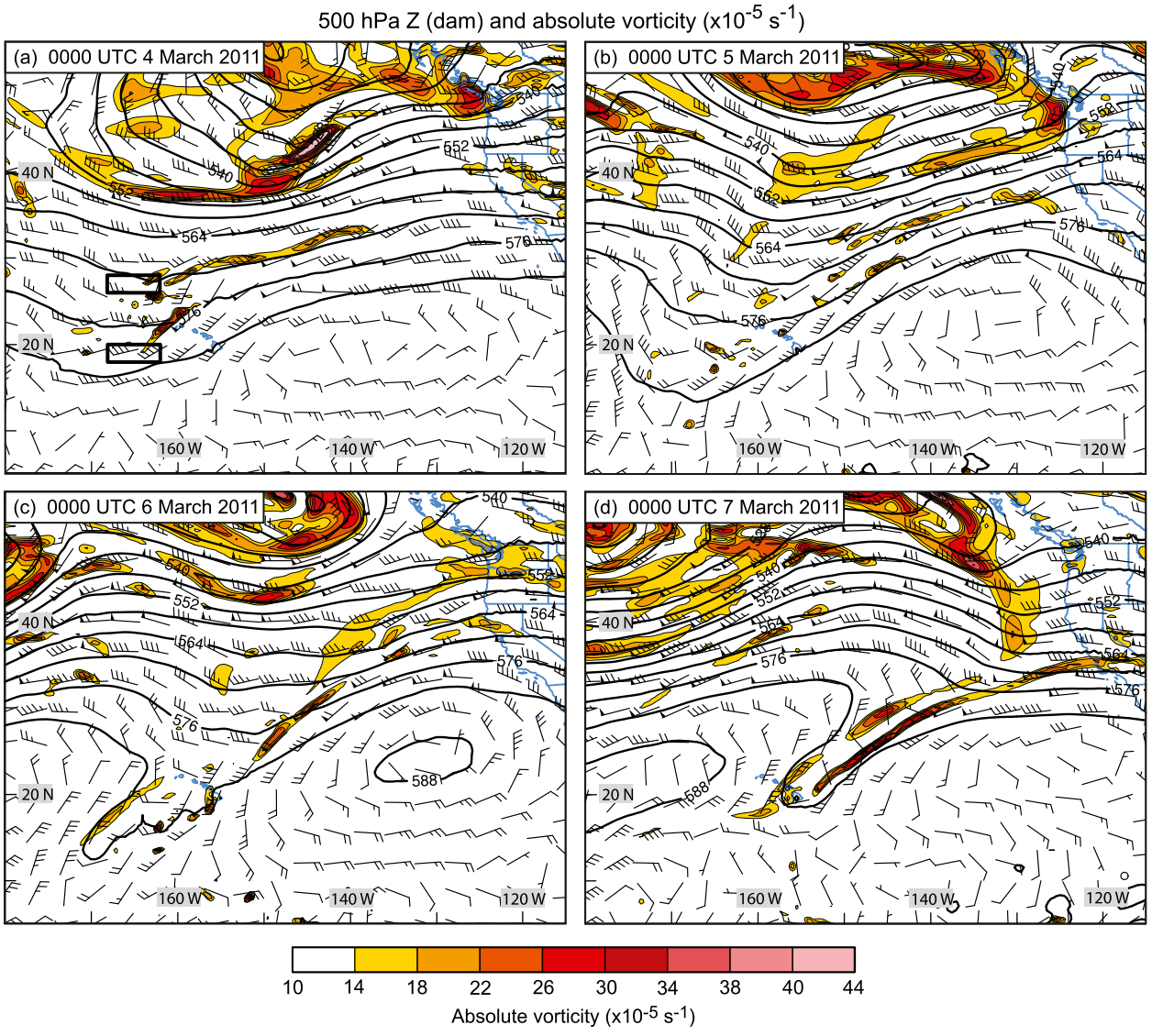

FIG. 4. As in Fig. 3, but for 500-hPa geopotential height (dam; black contours), absolute vorticity ($\times 10^{-5}\,s^{-1}$; color scale at bottom), and wind velocities.

adjusted, because the IWV values from these drops mapped quite well onto the IWV imagery at 1921 UTC. This agreement arose largely because of the close temporal match between the dropsondes and the imagery, and because the leading nose of the AR was moving perpendicular to the flight track. The remaining drops, from 2220 UTC 3 March to 0302 UTC 4 March, were time-to-space adjusted onto Fig. 9 using the AR phase velocity given above. After the adjustment, those dropsonde IWV values closely matched their SSMIS counterparts. Also, after the adjustment, the kinematic budget box shifted poleward from the core of the AR plume of largest IWV (Figs. 8 and 9a), although it remained in a moist environment with IWV $>$ 4 cm. Low-level (i.e., 925 hPa) southwesterly flow was observed in the equatorward half of the AR plume while northeasterly flow covered the region north of there. The budget box coincided with a sharp wind shear line separating these two airstreams. Companion SSMIS images of CLW and RR (Figs. 9b,c) reveal that the greatest concentration of cloud water and the heaviest rains resided south and east of the budget box within the AR.

Dropsonde θ_e analyses at four levels (Fig. 10) provide three-dimensional thermodynamic context to the SSMIS imagery. At 925 and 850 hPa (Figs. 10a,b), the leading nose of the AR exhibited warm-frontal characteristics, whereas farther west across the budget box the

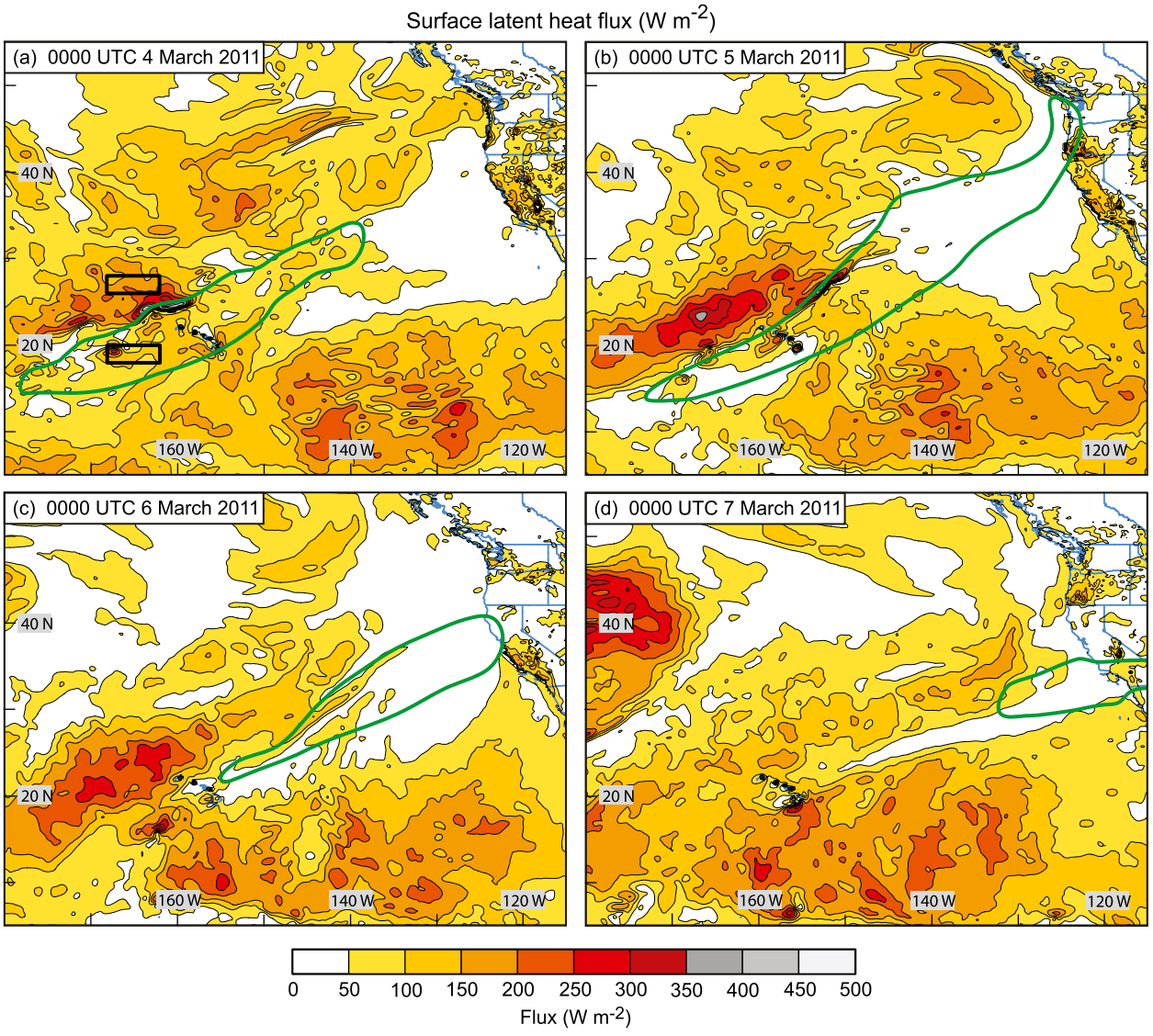

FIG. 5. As in Fig. 3, but for surface latent heat flux ($W\,m^{-2}$; color scale at bottom). The bold green outline in each panel marks the IVT isopleth of $250\,kg\,s^{-1}\,m^{-1}$ (from Fig. 2) associated with the AR of interest.

sharp wind shear line marked a cold-frontal boundary. Farther south, the southwesterly AR flow contained a broad region of warm, moist $\theta_e > 332$ K. The analysis at 700 hPa (Fig. 10c) resided above the shallow post-cold-frontal northeasterly flow, and the moist baroclinic zone and concomitant wind direction shift were weaker than below. A narrow zone of warm, moist $\theta_e > 324$ K in west-southwesterly flow marked the AR at this level. Similar characteristics were observed at 500 hPa (Fig. 10d). In addition, the cyclonically curved flow aloft reflected the southern branch shortwave trough captured in the CFSR analysis at 500 hPa (i.e., Fig. 4a).

The vertical structure across the AR is highlighted in a cross section along line northwest–southeast (NW–SE) in Figs. 9 and 10, based on 17 dropsondes spanning ~1800 km between 0003 and 0302 UTC 4 March 2011 (Fig. 11). An analysis of potential temperature (θ; Fig. 11a) shows weakly sloping cold-frontal isentropes below 850 hPa across the budget box, with southwesterly (northeasterly) flow on its equatorward (poleward) side. Aloft, more substantial sloping isentropes associated with an upper cold front descended southeastward from the tropopause and crossed the box between 550 and 400 hPa, with a broad cyclonic wind shift from southwesterly to northwesterly marking the shortwave trough (e.g., Fig. 4a). Far to the southeast, a sharp static-stability lamina at 850 hPa separated low-level southeasterly flow from southwesterlies aloft and marked the

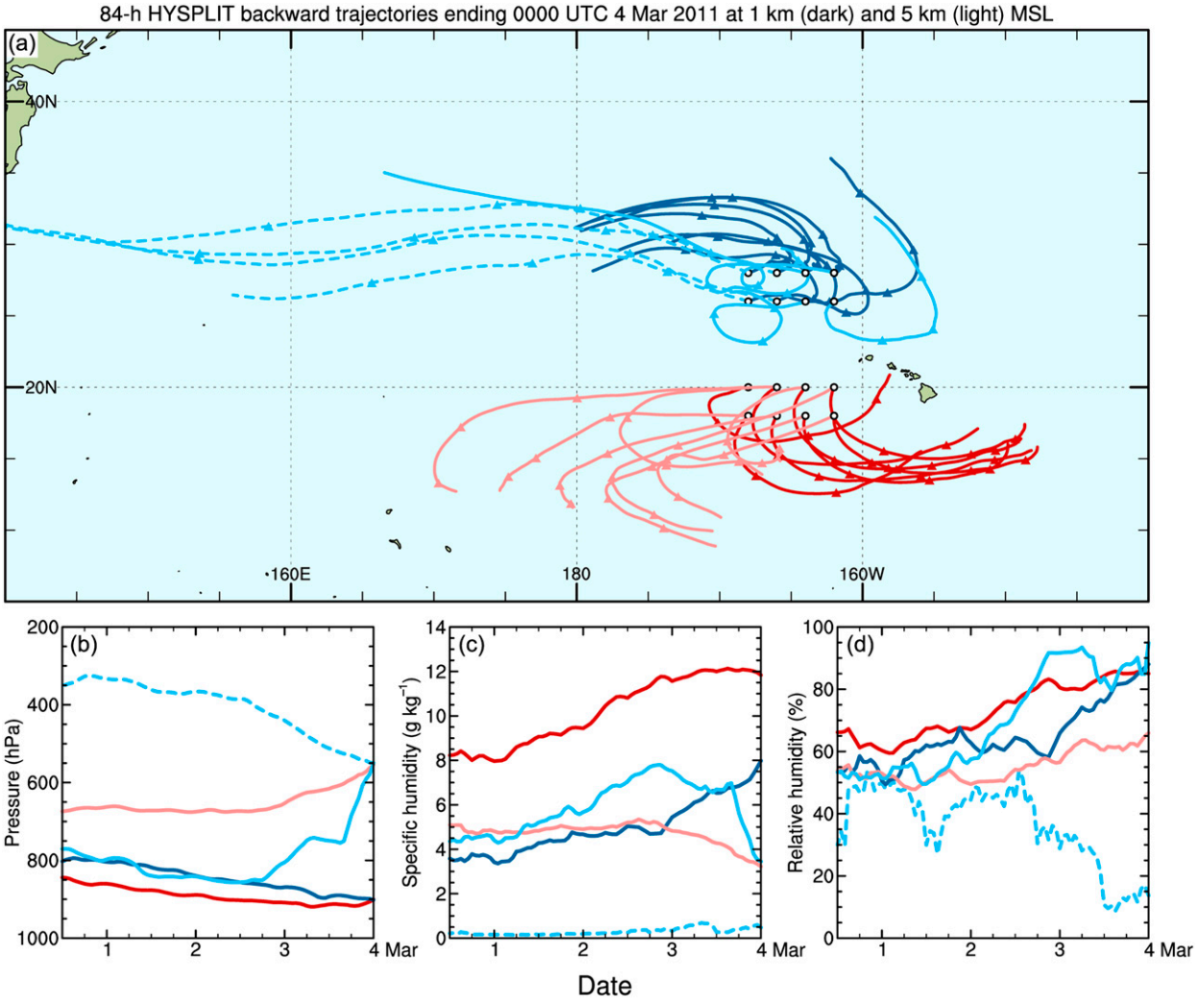

FIG. 6. (a) The 2 × 4 arrays (2° latitude × 2° longitude resolution) of 84-h backward air parcel trajectories ending at 0000 UTC 4 Mar 2011 (white circles), computed from the GDAS analyses using the HYSPLIT model. Blue (red) represents the northern (southern) array. The bright (dim) colors denote trajectories ending at 1 km (5 km) MSL. The dim blue solid (dashed) lines represent the 5-km trajectories on the eastern (western) half of the northern array. The triangles mark the air parcel positions at 24-h increments backward from the end time. (b) Time series of average hourly air pressure (hPa) along the five sets of colored trajectories shown in (a), from 1200 UTC 28 Feb to 0000 UTC 4 Mar 2011. (c) As in (b), but for water vapor specific humidity (g kg^{-1}). (d) As in (b), but for relative humidity (%).

trade wind inversion (described in section 5). A companion cross section of θ_e and RH (Fig. 11b) documents deep upright moist baroclinicity (from the surface to ~350 hPa) extending poleward from the budget box into a drier post-cold-frontal region. On the warm side of the box, a narrow (~300 km wide) band of nearly saturated air up to ~500 hPa coincided with warm, moist ($\theta_e >$ 332 K) conditions in a potentially unstable environment. Farther southeast, dry air sat atop the shallow, moist trade wind flow.

An analysis of water vapor specific humidity (q) and AR-parallel isotachs (U; directed from 235°) (Fig. 11c) underscores the enhanced low-level water vapor content (8–16 g kg^{-1}) and southwesterly flow (>~15 m s^{-1}) in the AR environment on the equatorward side of the budget box. A strong low-level U gradient across the box marked the shallow cold-frontal boundary. Aloft, a 35 m s^{-1} southwesterly jet centered at ~285 hPa accompanied the upper cold front described earlier. The U and q fields were combined into a 50-hPa-resolution analysis of horizontal AR-parallel water vapor flux (Fig. 11d) using the technique described in Ralph et al. (2004). Strong fluxes of >50 kg s^{-1} m^{-1} highlight a ~450-km-wide AR corridor of moist southwesterly flow up to ~500 hPa on the equatorward side of the budget box, while shallower (below ~850 hPa) but comparably strong vapor fluxes in the opposite direction resided within the box and on its poleward side in the moist

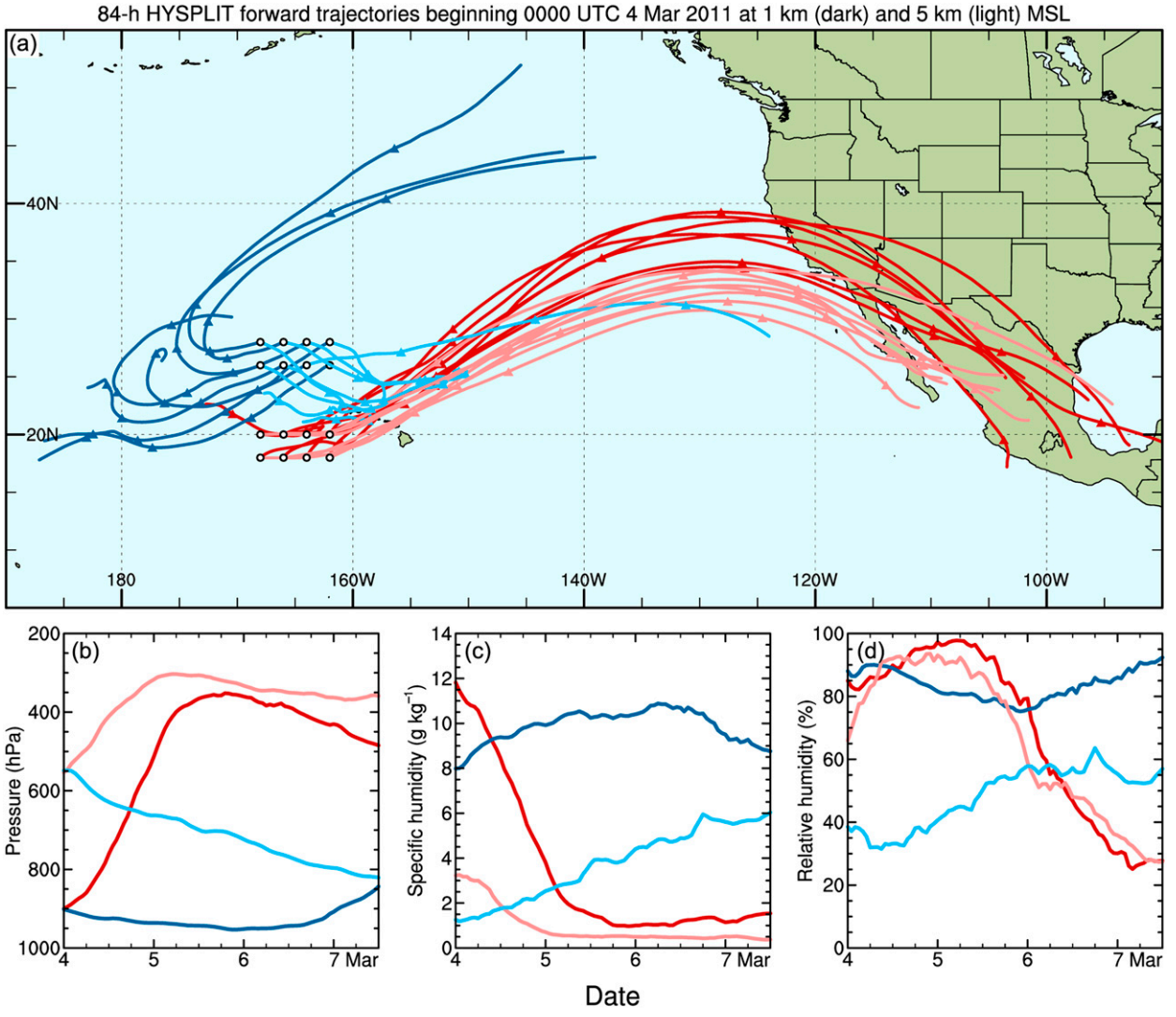

FIG. 7. As in Fig. 6, but for 84-h forward air parcel trajectories beginning at 0000 UTC 4 Mar 2011. The triangles mark the air parcel positions at 24-h increments forward from the start time.

post-cold-frontal northeasterly flow. The vertical integral of these fluxes (i.e., the IVT) between 1000–200 hPa is shown in Fig. 11e together with the corresponding IWV. A narrow IVT maximum of ~700 kg s^{-1} m^{-1} within the AR coincided with a much broader IWV maximum of 5 cm. The IVT decreased sharply poleward of the peak due to the strong southwestward-directed fluxes on the cold side of the front, whereas the IWV tailed off slowly due to persistent large water vapor content in the shallow northeasterlies.

Mutual inspection of Figs. 11d,e reveal that IVT values exceeding 250 kg s^{-1} m^{-1} capture the deep-layer, northeastward-directed water vapor transport associated with the AR. Despite the fact that this AR is characterized by a distinct IWV plume in the SSMIS satellite imagery (Figs. 1 and 9a), it is difficult to define the AR using a minimum IWV threshold due to very moist lower-tropospheric conditions in the subtropics (e.g., Fig. 11c), which then yield large background values of IWV. In contrast, ARs in the midlatitudes generally exhibit a well-defined minimum IWV threshold of ~2 cm (e.g., Ralph et al. 2004) because the background lower-tropospheric conditions, and hence the background IWV, is much drier than in the subtropics.

The AR structures and peak IVT values described above conform generally to those of strong ARs occurring over the midlatitudes and subtropics (e.g., Ralph et al. 2004, 2005, 2011; Neiman et al. 2008a, 2008b, 2011, 2013), although this case possessed the largest IWV and generally weaker winds. Also, the shallow, strong negative water vapor fluxes observed on the cold side of this AR was documented to a lesser extent in only the one other

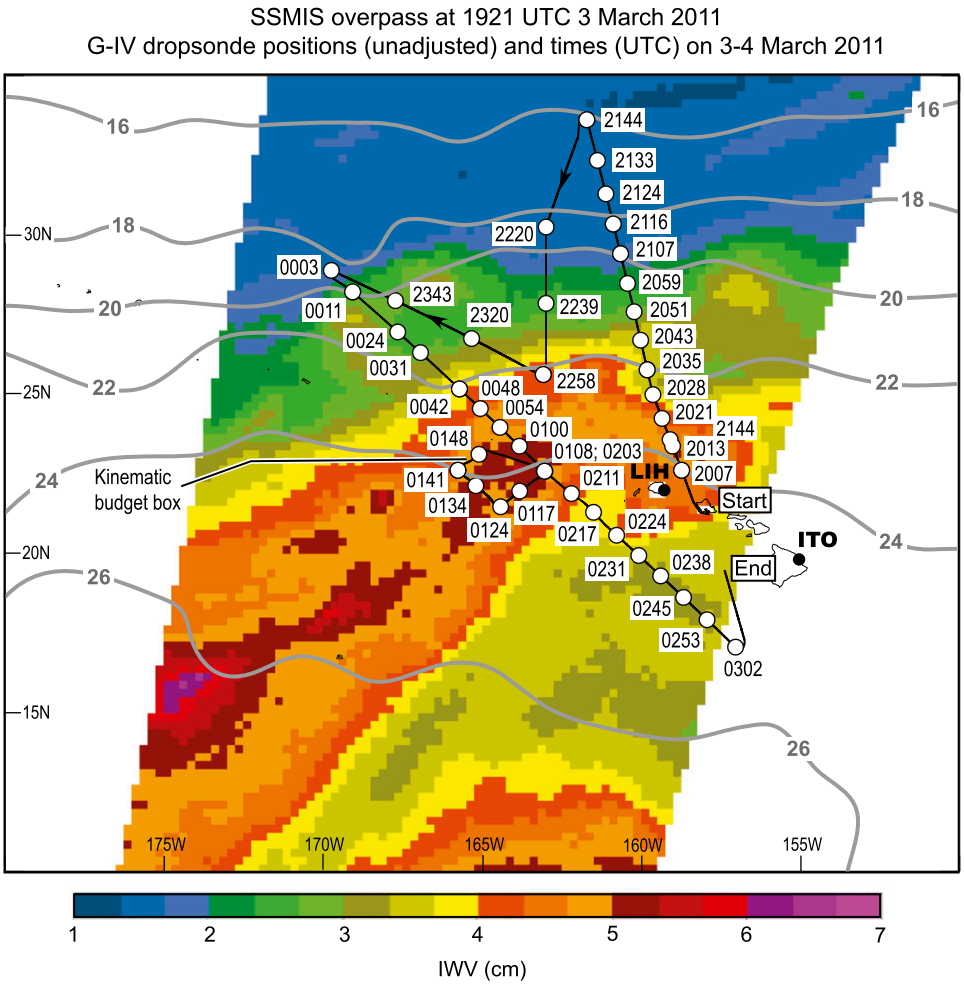

FIG. 8. Satellite image swath at 1921 UTC 3 Mar 2011 of IWV (cm; color scale at bottom) from the SSMIS. The unadjusted G-IV flight track is superimposed, along with dots marking the positions and times of the dropsonde releases late on 3 Mar (2007–2343 UTC) and early on 4 Mar (0003–0302 UTC) 2011. The operational rawinsonde locations at Lihue (LIH) and Hilo (ITO) on Hawaii are shown. Manually smoothed satellite-derived sea surface temperatures (°C; contours) from the Reynolds et al. (2007) daily 0.25° × 0.25° resolution optimally interpolated infrared product are also shown.

subtropical cross section from 25 March 2005 (Ralph et al. 2011), where shallow, moist post-cold-frontal northerly flow was observed. The midlatitude cross-section counterparts cited above contained weak but positive vapor fluxes on the cold side of the ARs in a region of weak and relatively dry southwesterly flow. Unlike all other previously published cases, the AR studied here exhibited a much sharper decrease in IVT than IWV on the poleward side of the AR.

In addition to the dropsonde observations in Fig. 11e, gridded IVT and IWV are shown from four global reanalysis datasets: the CFSR, the Interim European Centre for Medium-Range Weather Forecasts (ECMWF) Re-Analysis (ERA-Interim) product (~80-km horizontal resolution; Dee et al. 2011), NASA's Modern-Era Retrospective Analysis for Research and Applications (MERRA; ~65-km resolution; Rienecker et al. 2011), and the NCEP–National Center for Atmospheric Research Reanalysis Project (NNRP; ~250-km resolution; Kalnay et al. 1996). The reanalysis traces are valid at 0000 UTC 4 March 2011 and were time-to-space adjusted to match the observed cross section using the phase velocity of 6.5 m s^{-1} from 313°. The three fine-resolution reanalysis datasets align generally with the observations over the data-sparse Pacific, which should be expected given that the dropsonde data were transmitted in real time via the Global Telecommunications System and assimilated into the model analyses (from which the reanalyses are derived). Nevertheless, the IWV and IVT maxima in the AR are underestimated in

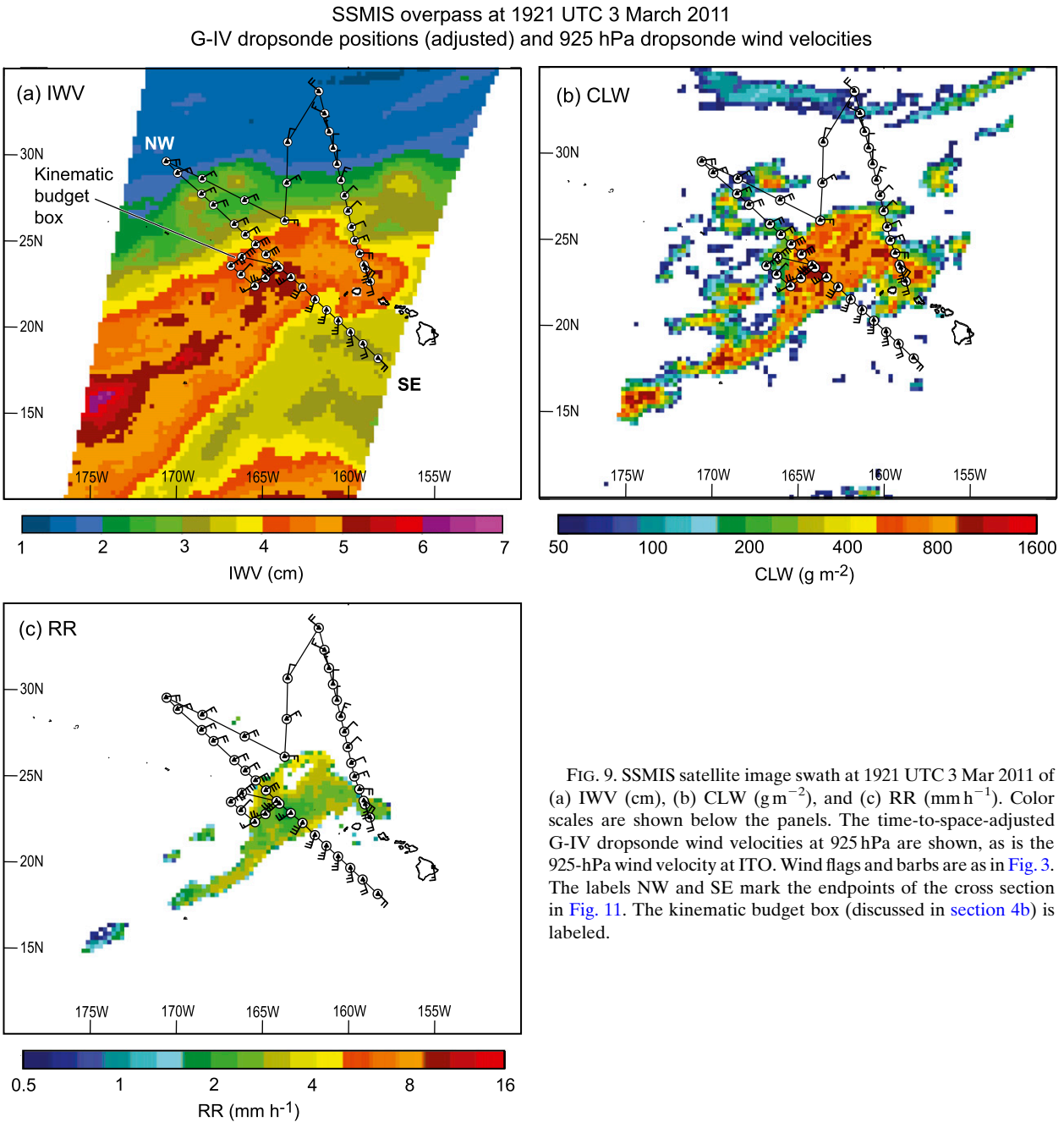

FIG. 9. SSMIS satellite image swath at 1921 UTC 3 Mar 2011 of (a) IWV (cm), (b) CLW ($g\,m^{-2}$), and (c) RR ($mm\,h^{-1}$). Color scales are shown below the panels. The time-to-space-adjusted G-IV dropsonde wind velocities at 925 hPa are shown, as is the 925-hPa wind velocity at ITO. Wind flags and barbs are as in Fig. 3. The labels NW and SE mark the endpoints of the cross section in Fig. 11. The kinematic budget box (discussed in section 4b) is labeled.

these reanalysis datasets, especially for the ERA-Interim and MERRA, while the ERA-Interim and MERRA also underestimate the sharpness of the IVT gradient across the shallow frontal shear zone and they place the AR too far southeast. Also, vertical details contained in companion reanalysis cross sections (not shown) differ from those in Figs. 11a–d. The coarse-grain NNRP provides the least favorable depiction of the AR. Based on these comparisons, gridded datasets may have difficulty accurately depicting the position and/or intensity of ARs over data-sparse oceans. This shortcoming could present challenges in accurately forecasting extreme precipitation and flooding associated with landfalling ARs, as was demonstrated in Ralph et al. (2011). Given the better performance of the CFSR here, subsequent reanalysis comparisons with dropsonde data will be limited to the CFSR.

b. *Budget-box diagnostics*

A sequential set of eight dropsondes were released in a ~200-km-wide box formation on the poleward edge of

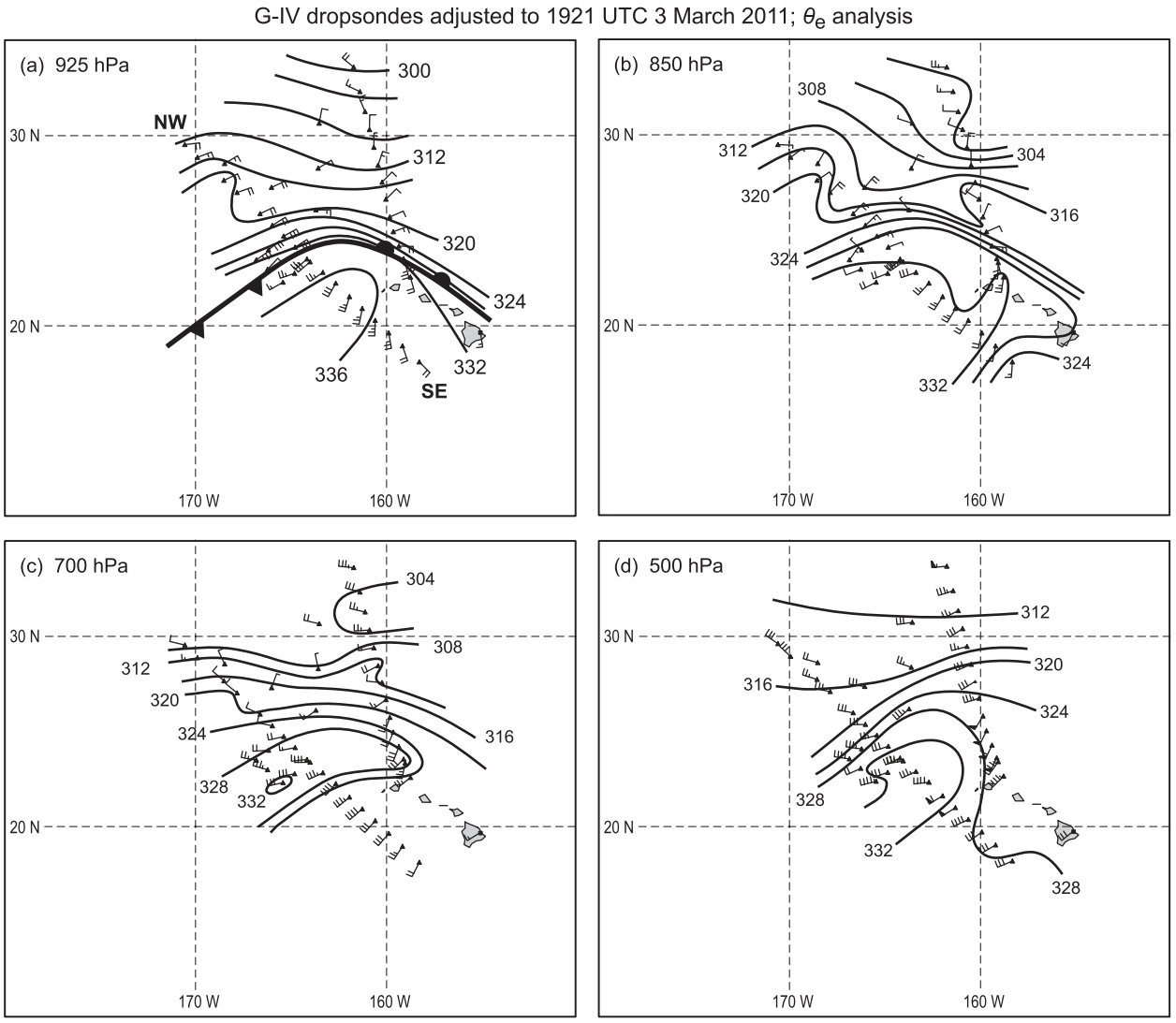

FIG. 10. Time-to-space-adjusted G-IV dropsonde wind velocities (wind flags and barbs are as in Fig. 3) and θ_e contours (K) at 1921 UTC 3 Mar 2011 on the following pressure levels: (a) 925, (b) 850, (c) 700, and (d) 500 hPa. A 925-hPa frontal analysis using standard notation is included in (a). The labels NW and SE in (a) mark the endpoints of the cross section in Fig. 11.

the AR and across the shallow cold-frontal wind shear line between 0054 and 0203 UTC 4 March (Figs. 8–10). The data from each dropsonde were layer averaged onto a 50-hPa-resolution vertical grid, from 975 to 175 hPa. Then, the following kinematic variables were diagnosed at each pressure level for the area within the budget box using the trapezoidal line-integral technique described in McBride et al. (1989):

$$\text{Area} = A = \frac{1}{2}\oint(x\,dy - y\,dx), \tag{1}$$

$$\text{Mass flux divergence} = \nabla\cdot\mathbf{V} = \frac{1}{A}\oint(u\,dy - v\,dx), \tag{2}$$

$$\text{Sensible heat flux divergence} = \nabla\cdot(\theta\mathbf{V}) = \frac{1}{A}\oint(\theta u\,dy - \theta v\,dx), \tag{3}$$

$$\text{Water vapor flux divergence} = \nabla\cdot(q\mathbf{V}) = \frac{1}{A}\oint(qu\,dy - qv\,dx), \tag{4}$$

and

$$\text{Relative vorticity} = \nabla\times\mathbf{V} = \frac{1}{A}\oint(u\,dx + v\,dy), \tag{5}$$

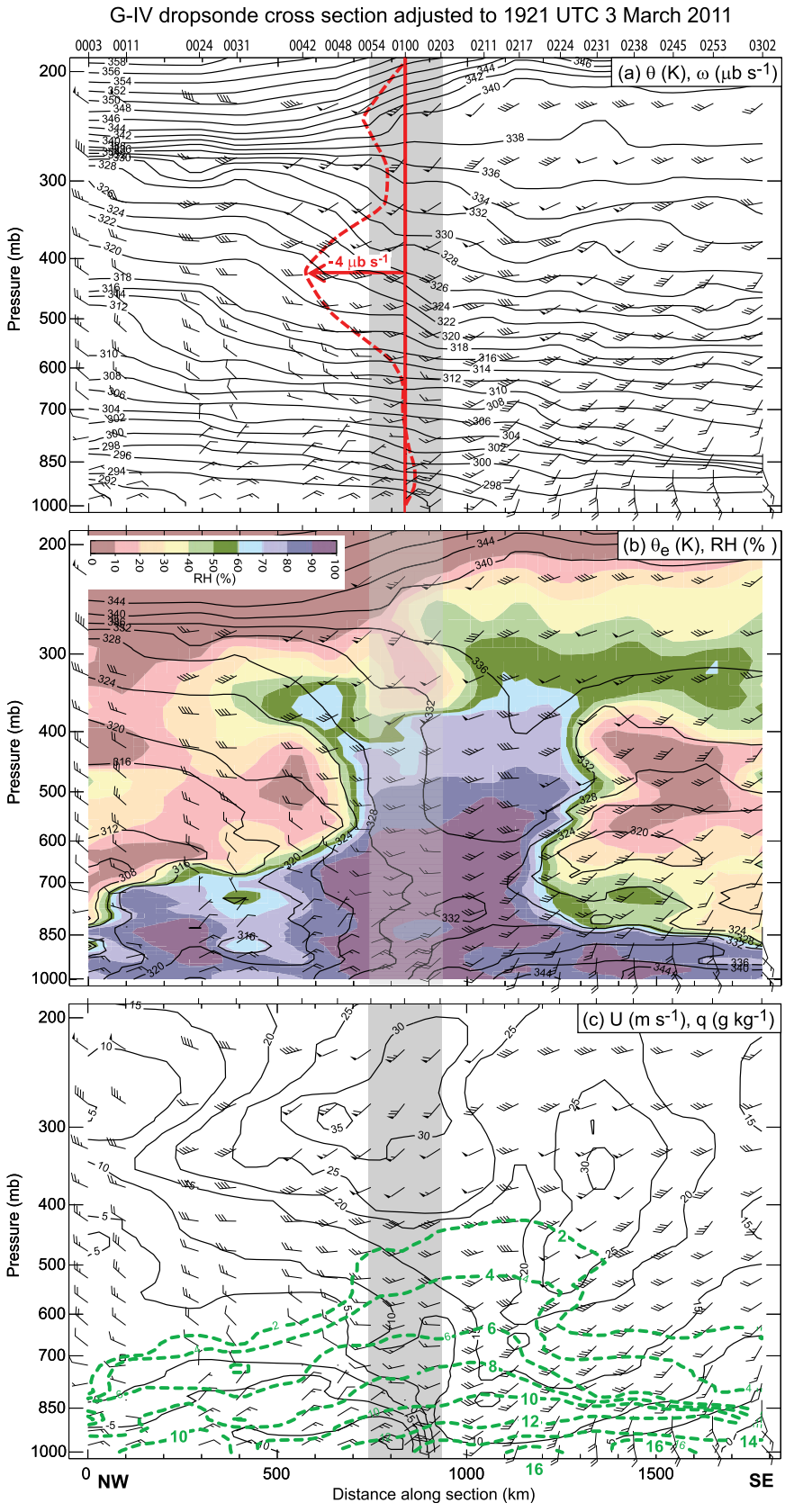

FIG. 11. (*Continued*)

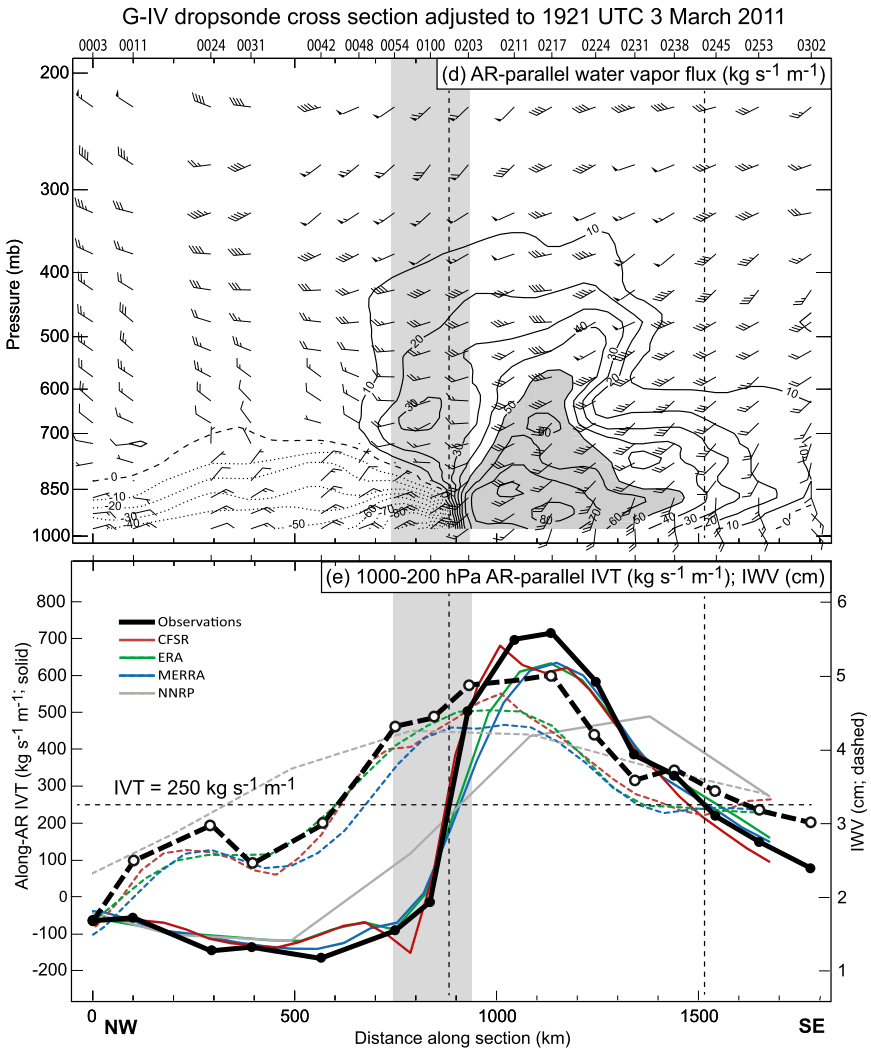

FIG. 11. Time-to-space-adjusted G-IV dropsonde cross sections along the baseline NW–SE in Figs. 9 and 10 at 1921 UTC 3 Mar 2011: (a) θ (K; black contours at 2-K interval); (b) θ_e (K; black contours at 4-K interval) and relative humidity (%; color contours); (c) AR-parallel isotachs ($\mathrm{m\,s^{-1}}$; black contours, directed from 235° (i.e., approximately into the page) and water vapor specific humidity ($\mathrm{g\,kg^{-1}}$; green contours); (d) AR-parallel horizontal water vapor flux ($\mathrm{kg\,s^{-1}\,m^{-1}}$; black contours, directed from 235°; shading $>50\,\mathrm{kg\,s^{-1}\,m^{-1}}$); and (e) IWV (cm; black dashed) and 1000–200-hPa AR-parallel IVT ($\mathrm{kg\,s^{-1}\,m^{-1}}$; black solid), with reanalysis counterparts also shown (see key). Wind flags and barbs in (a)–(d) are as in Fig. 3. The gray-shaded bar in each panel marks the lateral domain of the kinematic budget box labeled in Fig. 9a. The vertical velocity profile ($\mu\mathrm{b\,s^{-1}}$; red dashed) shown in (a) is derived from the observed budget-box diagnostics. The vertical dashed lines in (d) and (e) correspond to observed IVT = $250\,\mathrm{kg\,s^{-1}\,m^{-1}}$, which is the horizontal dashed line in (e). Dropsonde times (UTC) on 4 Mar 2011 are shown at the top, and the distance (km) along the cross section is indicated on the bottom.

where the layer-averaged variables at each level of each sonde position (x, y) are as follows: $\mathbf{V}$ is the wind velocity vector; u and v are the zonal and meridional wind components, respectively; θ is potential temperature; and q is water vapor specific humidity. Vertically integrating the mass flux divergence profile via the continuity equation gives a box-averaged vertical velocity profile:

$$\omega = \frac{\partial p}{\partial t} = -\int_{p_1}^{p_2} (\nabla \cdot \mathbf{V})\, dp, \tag{6}$$

where p_1 and p_2 are the pressure at adjacent levels, ω has units of $\mu\mathrm{b\,s^{-1}}$, and hydrostatic balance is assumed implicitly. A mass-balanced correction was applied at each level of the diagnosed divergence profiles [Eqs. (2)–(4)]

to ensure that ω was zero at the lowest and highest level. Box-averaged profiles of the observed thermodynamic and wind data were also calculated.

Box-averaged profiles of temperature and dewpoint (Fig. 12a) show moist conditions and a high melting level (4 km MSL) in the warm air mass. Companion profiles of θ and θ_e (Fig. 12b) and RH (Fig. 12c) reveal the presence of potential instability in the saturated, above-freezing layer below 4 km MSL. Box-averaged specific humidity of 11–13 g kg^{-1} in the lowest 1 km (Fig. 12d) further highlight the moist character of this air mass. Profiles of averaged wind direction and wind speed (Figs. 12e,f) show a prominent vertical shear layer separating shallow post-cold-frontal northeasterly flow from the southwesterlies aloft, although the box averaging muted the strength of the vertical shear found on the cold side of the front. The eight dropsonde profiles that comprise the box averages are shown as gray-shaded curves in Fig. 12 and underscore the overall representativeness of those averages, save the low-level wind directions below 2 km MSL across the frontal zone. Corresponding mean profiles from the CFSR within the budget-box domain (Fig. 12) conform generally to their observed counterparts, save for the relative humidity and specific humidity profiles which are drier below ~5 km MSL (i.e., within the altitude range of the AR) and more moist aloft. The dry bias in the lower troposphere is a common attribute for all four reanalysis products in the AR environment, using IWV as the comparison metric (Fig. 11e).

The observed kinematic budget-box diagnostics are presented in Fig. 13. The profile of relative vorticity (Fig. 13a) contains a shallow layer of strong cyclonic vorticity centered at 0.75 km MSL across the shear line separating the post-cold-frontal northeasterlies from the prefrontal southwesterlies (Figs. 10 and 11). Aloft, weaker cyclonic vorticity marks the cyclonically curved flow of the upper-level, southern branch, baroclinic shortwave trough (Fig. 4a). The profile of mass-balanced divergence (Fig. 13b) shows values near zero in the lowest 4 km MSL. Modest convergence between 4 and 7 km MSL is tied to the shortwave trough aloft. A companion ω profile (Fig. 13b) shows near-neutral vertical motions through 4 km MSL, then ascent aloft, attaining a maximum magnitude of $-4\,\mu$b s^{-1} at ~7 km MSL. For context, the ω profile was placed on the θ cross section in Fig. 11a. The weak vertical motion below 4 km overlaps a region of nearly horizontal isentropes, whereas the upward motion aloft coincides with the slantwise isentropes of the upper cold front and trough. Profiles of water vapor and sensible heat flux divergence (Fig. 13c) contain weak values below 4 km MSL (save for the lowest level) and larger values aloft. Vertically integrating the water vapor flux divergence profile yields a column-integrated specific humidity decrease of 8.51 g kg^{-1} day^{-1}, which converts to a daily change in IWV of -0.43 cm based on IWV = $(q/g)\Delta p$ (Saucier 1955), where g is gravity and Δp is 50 hPa. Based on dropsonde measurement uncertainties, maximum uncertainties for the kinematic diagnostics for this case are modest relative to the diagnostic magnitudes: $\pm 0.65 \times 10^{-5}$ s^{-1} for vorticity, $\pm 0.13 \times 10^{-5}$ s^{-1} for divergence, $\pm 0.07\,\mu$b s^{-1} for ω, ± 1.19 g kg^{-1} day^{-1} for water vapor flux divergence (except ± 2.48 g kg^{-1} day^{-1} in the lowest layer), and 32.6 K day^{-1} for sensible heat flux divergence.

For reference, kinematic profiles from the CFSR in the budget-box domain are also shown in Fig. 13, where the kinematic values from the reanalysis grids were spatially averaged over the area of the budget box. The relative vorticity compares favorably with the observations, while the mass divergence and ω comparisons are modestly less favorable. The least favorable comparisons are with the water vapor and sensible heat flux divergence profiles. The daily change in IWV resulting from the CFSR water vapor flux divergence profile is 1.84 cm, which is opposite in sign and >4 times larger in magnitude than its observed counterpart. The kinematic quantities (Fig. 13) are more sensitive than the mean quantities (Fig. 12) to mesoscale gradients such as with the front and AR. Hence, one should expect poorer comparisons of the kinematic quantities, arising from reanalysis errors in position and/or intensity.

Sea surface sensible and latent heat fluxes were calculated in the budget box using near-surface (i.e., 10 m MSL) dropsonde measurements of temperature (T_{10}), water vapor specific humidity (q_{10}), density (ρ_{10}), and wind speed ($|\mathbf{V}_{10}|$), and satellite-derived sea surface measurements of temperature (T_{SST}; Fig. 8) and saturation specific humidity (q_{SST}). The bulk equations for the sea surface sensible and latent heat fluxes are

$$F_S = -\rho_{10} C_h C_p |\mathbf{V}_{10}|(T_{10} - T_{\mathrm{SST}}), \tag{7}$$

$$F_L = -\rho_{10} C_q L_c |\mathbf{V}_{10}|(q_{10} - q_{\mathrm{SST}}), \tag{8}$$

where C_h and C_q are the exchange coefficients for sensible heat flux and evaporation, respectively; C_p is the specific heat of dry air at constant pressure; and L_c is the latent heat of condensation. The exchange coefficients were computed from the widely utilized version 3.0 of the Coupled Ocean–Atmosphere Response Experiment bulk-flux algorithm (Fairall et al. 2003). These coefficients, which are dependent on the near-surface static stability and wind speed, have reduced the uncertainty in the bulk-flux calculations from 30% twenty years ago to ≤10% for the wind speeds observed in this case. The following box-averaged meteorological observations

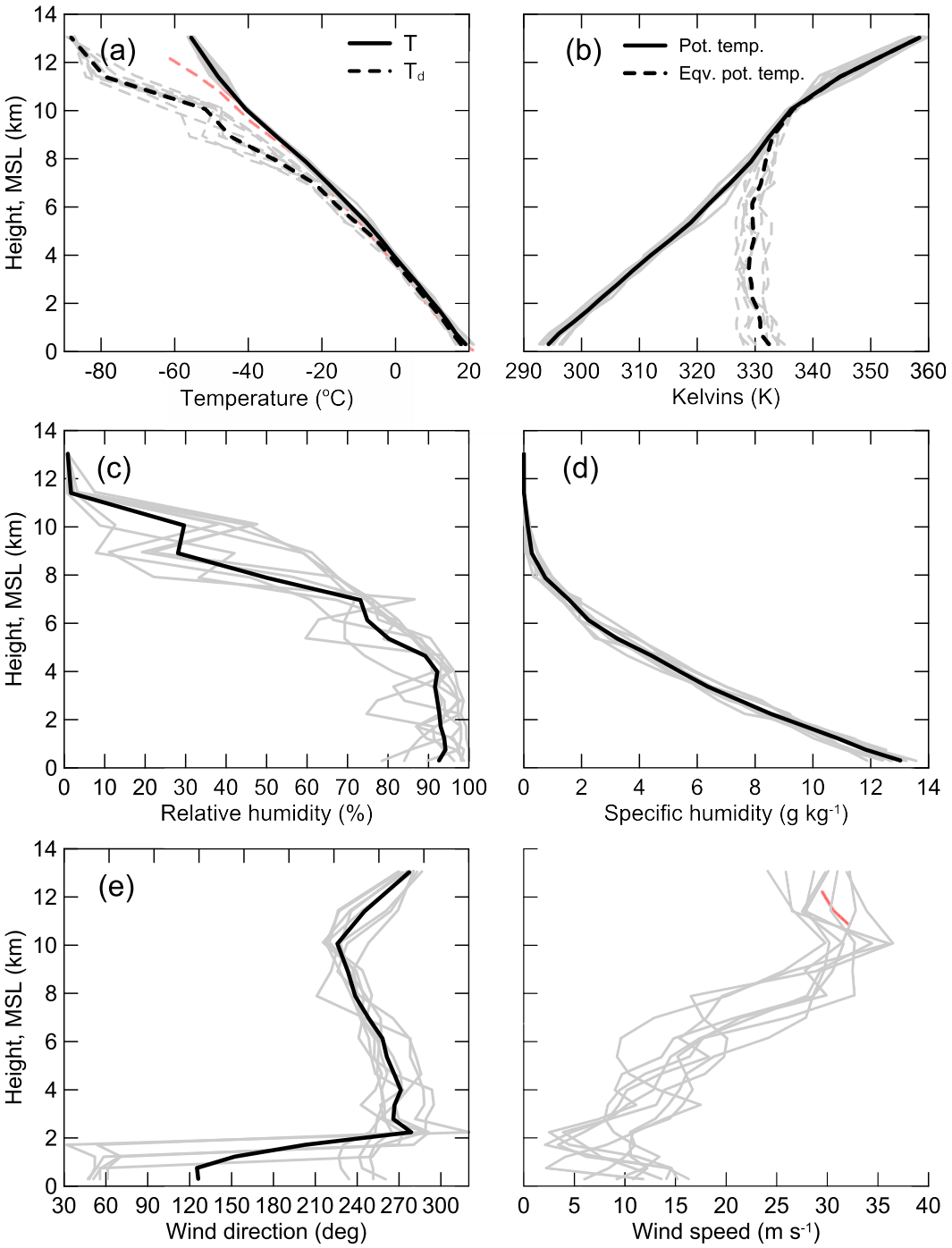
(a)
T
T_d
Height, MSL (km)
Temperature (°C)
(b)
Pot. temp.
Eqv. pot. temp.
Kelvins (K)
(c)
Relative humidity (%)
(d)
Specific humidity (g kg^{-1})
(e)
Wind direction (deg)
Wind speed (m s^{-1})

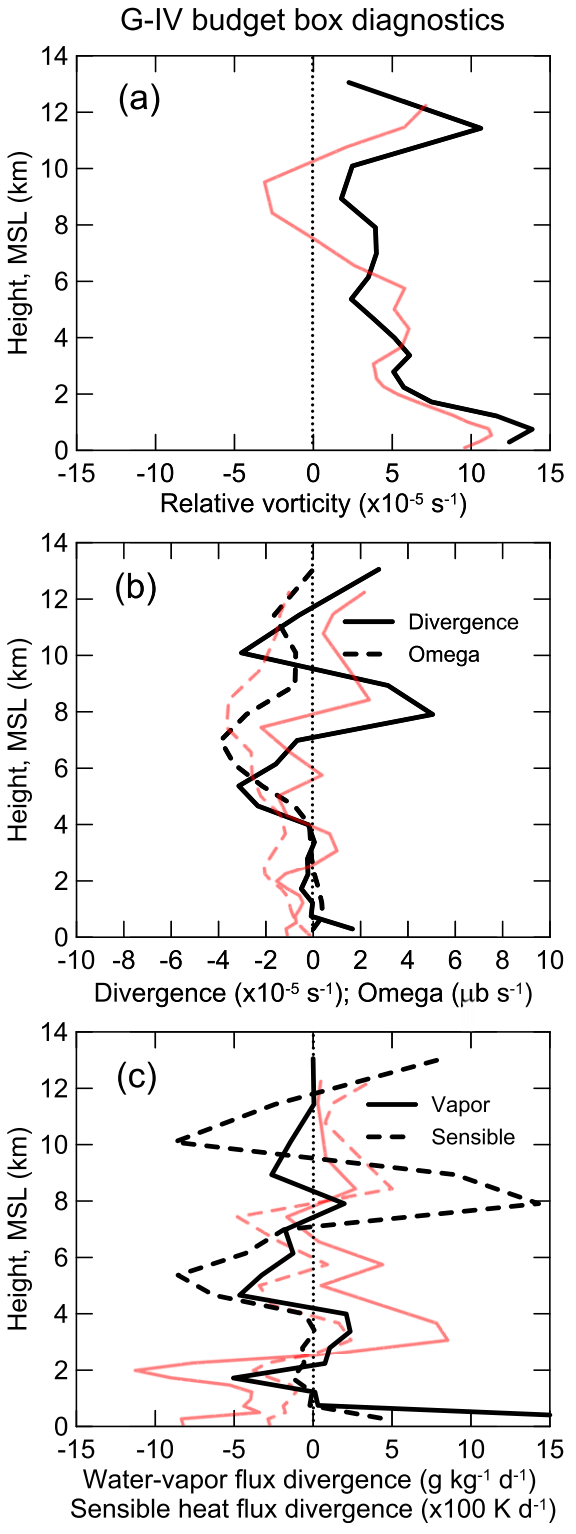

FIG. 13. Kinematic diagnostic profiles (black curves) derived from the eight G-IV dropsondes comprising the budget box labeled in Fig. 9a: (a) relative vorticity ($\times 10^{-5}\,s^{-1}$); (b) mass-balanced divergence ($\times 10^{-5}\,s^{-1}$; solid) and vertical velocity ($\mu b\,s^{-1}$; dashed); and (c) mass-balanced water vapor flux divergence ($g\,kg^{-1}\,day^{-1}$; solid) and sensible heat flux divergence ($\times 100\,K\,day^{-1}$). The vertical dotted line in each panel marks the 0 value. The red profiles represent the CFSR values in the budget-box domain.

were used to calculate the exchange coefficients and bulk fluxes: $T_{SST} = 24.0°C$, $q_{SST} = 18.40\,g\,kg^{-1}$, $|\mathbf{V}_{10}| = 11.2\,m\,s^{-1}$, $T_{10} = 21.4°C$, $q_{10} = 14.46\,g\,kg^{-1}$, $\rho_{10} = 1.19\,kg\,m^{-3}$, and $p = 1009.0\,hPa$. The resulting exchange coefficients are $C_h = 1.13 \times 10^{-3}$ and $C_q = 0.99 \times 10^{-3}$, and the bulk fluxes are $F_S = 40\,W\,m^{-2}$ and $F_L = 149\,W\,m^{-2}$. An F_L value of $149\,W\,m^{-2}$ contributes to a daily increase in IWV of $0.52\,cm^{-1}$, and these compare favorably with their CFSR counterparts (i.e., $159\,W\,m^{-2}$, 0.55 cm). The observed heat fluxes in the budget box are larger in the modestly cooler and drier low-level northeasterly flow (i.e., $F_S = 40$–$71\,W\,m^{-2}$, $F_L = 151$–$217\,W\,m^{-2}$) than in the warmer and more moist low-level southwesterlies (i.e., $F_S = 9$–$26\,W\,m^{-2}$, $F_L = 66$–$114\,W\,m^{-2}$). The latent heat fluxes diagnosed from the three dropsondes immediately northwest of the budget box (i.e., 0031–0048 UTC in Fig. 8) range between 152 and $206\,W\,m^{-2}$, similar to those in the north portion of the box, and they decrease to 88–$155\,W\,m^{-2}$ in the three northwestmost dropsondes (i.e., 0003–0024 UTC in Fig. 8) due to cooler underlying sea surface temperatures.

As a proof of concept, the observed daily change of IWV in the budget box is calculated by summing the three primary terms of the water budget: column-integrated water vapor flux divergence (−0.43 cm), sea surface evaporation (0.52 cm), and rain rate. A box-averaged rain-rate measurement of $1.7\,mm\,h^{-1}$ (i.e., $4.08\,cm\,day^{-1}$) from the SSMIS satellite image at 1921 UTC 3 March 2011 (Fig. 9c) yields a net daily IWV loss of 3.99 cm in the box, based on the summation of the three terms. Sequential SSMIS IWV imagery (Fig. 1) does not support this loss. Hence, it is likely that the large time lag of 5.5–6.6 h between the SSMIS and airborne observations, coupled with the fact that rain rates typically vary sharply in both space and time, yielded poor water budget results. A more accurate assessment of observed water budgets in future field campaigns will require enhanced rain-rate measurements from airborne radar that are time matched with the dropsonde observations. For comparison, the CFSR rain rate in the budget-box domain is $0.95\,mm\,h^{-1}$, thus yielding a net daily IWV increase of 0.11 cm. Although this result more closely matches the sequential satellite imagery, both the sea surface latent heat flux and rain rate in the CFSR are determined primarily by model output rather than from observations (e.g., Kalnay et al. 1996), so those results should be treated with caution.

5. Precipitation impacts in Hawaii

To first order, the climatological rainfall distribution over the Hawaiian Islands is the result of persistent, lower-tropospheric, east-northeasterly trade wind flow and the mean altitude of its capping inversion (e.g.,

Schroeder 1993; Giambelluca et al. 2013). The trade winds yield climatological rainfall patterns that are anchored to the terrain, with heavy amounts on east-facing mountain slopes beneath the trade wind inversion (positioned climatologically at ~2 km MSL; e.g., Cao et al. 2007) and light amounts on west-facing slopes and on the high summits above the inversion. The trade wind inversion, which limits cloud vertical development, arises due to large-scale subsidence in the dry upper troposphere in conjunction with low-level convective ascent (e.g., Riehl 1979; Albrecht 1984). It can erode episodically during periods of transient uplift associated with the passage of synoptic-scale disturbances (most frequently during the boreal cool season), resulting in deep-layer clouds and heavy precipitation that reach the high summits. These transient disturbances can also bring low-level southwesterly flow and orographic precipitation enhancement to the normally dry side of the islands, and are often referred to as kona storms (Simpson 1952; Otkin and Martin 2004).

For the AR storm studied here, Kauai received by far the greatest rainfall of all Hawaii's islands and will therefore be the focus of this section. Kauai is an island of orographically dominated rainfall extremes, ranging from ~10 000 mm annually on its 1544-m-high point of Mt. Waialeale (considered one of the wettest spots measured on Earth) to $<500\ \text{mm yr}^{-1}$ near the town of Kekaha, Hawaii, situated only 25 km southwest of the peak (e.g., Giambelluca et al. 2013; http://rainfall.geography.hawaii.edu). The north and east sides of Kauai are generally much wetter than the south and west sides due to persistent, moist, onshore trade winds.

Figure 14 shows four consecutive 24-h rain gauge accumulation maps on Kauai spanning the period 1200 UTC 2 March–1200 UTC 6 March 2011. Measured rainfall ending 1200 UTC 3 March was focused on the normally wet east side of the island. During the two follow-on 24-h periods, heavy rain fell across much of the island, including on the normally dry southwest side. For the last 24-h period ending 1200 UTC 6 March, heavy rains were again confined to the normally wet trade wind side of Kauai. Large 4-day totals of 200–367 mm were maximized on the normally wet side of the island and atop centrally located Mt. Waialeale. Given Kauai's widely varying rainfall climatology, Fig. 14 also shows the daily accumulations in a climatology normalized sense, which we define as the absolute 24-h total at each gauge divided by the daily-average total prorated from the March monthly climatology at that gauge. Based on those numbers, two things stand out: 1) the wet side of the island received impressive daily totals that were 5 to nearly 20 times greater than the climatological values, and 2) the dry side of the island recorded climatology normalized values that matched or surpassed their wet-side counterparts, despite the fact that the absolute accumulations there were significantly less for the most part.

Data collected from sequential operational rawinsondes launched at Lihue, Kauai (Figs. 15 and 16; LIH in Fig. 14), mirror the nearby G-IV dropsonde observations (Fig. 12) and highlight the local meteorology during the period of interest. A skew T–log$p$ plot at 0000 UTC 3 March 2011 (Fig. 15a) shows shallow, moist trade winds capped by dry southwesterlies aloft. By 0000 UTC 4 March (Fig. 15b), moistening southwesterly flow extended down to the surface and increased the IWV from 2.56 to 3.88 cm as the AR approached the island from the northwest (e.g., Fig. 2), although dry air persisted aloft. Twelve hours later (Fig. 15c), moist southwesterly flow in the AR core encompassed the entire troposphere, with IWV increasing further to 4.73 cm. By 0000 UTC 5 March (Fig. 15d), shallow northeasterlies returned beneath moist southwesterly AR flow aloft, and IWV decreased to a still moist 3.9 cm. These conditions persisted through 1200 UTC 5 March (Fig. 15e), although the northeasterly flow deepened. By 1200 UTC 6 March (Fig. 15f), the AR had moved beyond Hawaii (Fig. 2) and a more typical trade wind inversion reappeared; IWV decreased dramatically to 2.7 cm due to drying aloft.

Figure 16 shows additional perspective from the four LIH soundings in the AR between 0000 UTC 4 March and 1200 UTC 5 March 2011. Profiles of water vapor transport (Fig. 16a) for the earlier two times reveal positive AR-parallel fluxes (directed from 235°) in the lowest 7 km, with the strongest values below the top of Mt. Waialeale. The 1000–200-hPa IVT increased from 452 to $900\ \text{kg s}^{-1}\,\text{m}^{-1}$ as the core of the AR made landfall. The latter two soundings show a change in sign of the low-level AR-parallel vapor fluxes in response to the reestablishment of shallow northeasterly flow in the moist airstream. The IVT eventually changed sign as the strengthening low-level southwestward-directed fluxes more than compensated for the weakening northeastward-directed fluxes aloft. Companion profiles of θ and θ_e (Fig. 16b) reveal potential instability in the lowest 3 km MSL, which extends far above the island's highest terrain. The instability below 3 km is quantified with profiles of dry and moist Brunt–Väisälä frequency (Figs. 16e,f), which show stable conditions for an unsaturated atmosphere and neutral to unstable conditions for a saturated atmosphere. ARs with similar static stability characteristics have been observed in midlatitudes (e.g., Ralph et al. 2005, 2011; Neiman et al. 2008b, 2011, 2013). The companion RH profiles (Fig. 16c) show an essentially saturated atmosphere (RH $>$ 90%) in the lowest 2 km. Less than 400 m of lift was required for the potential instability in this

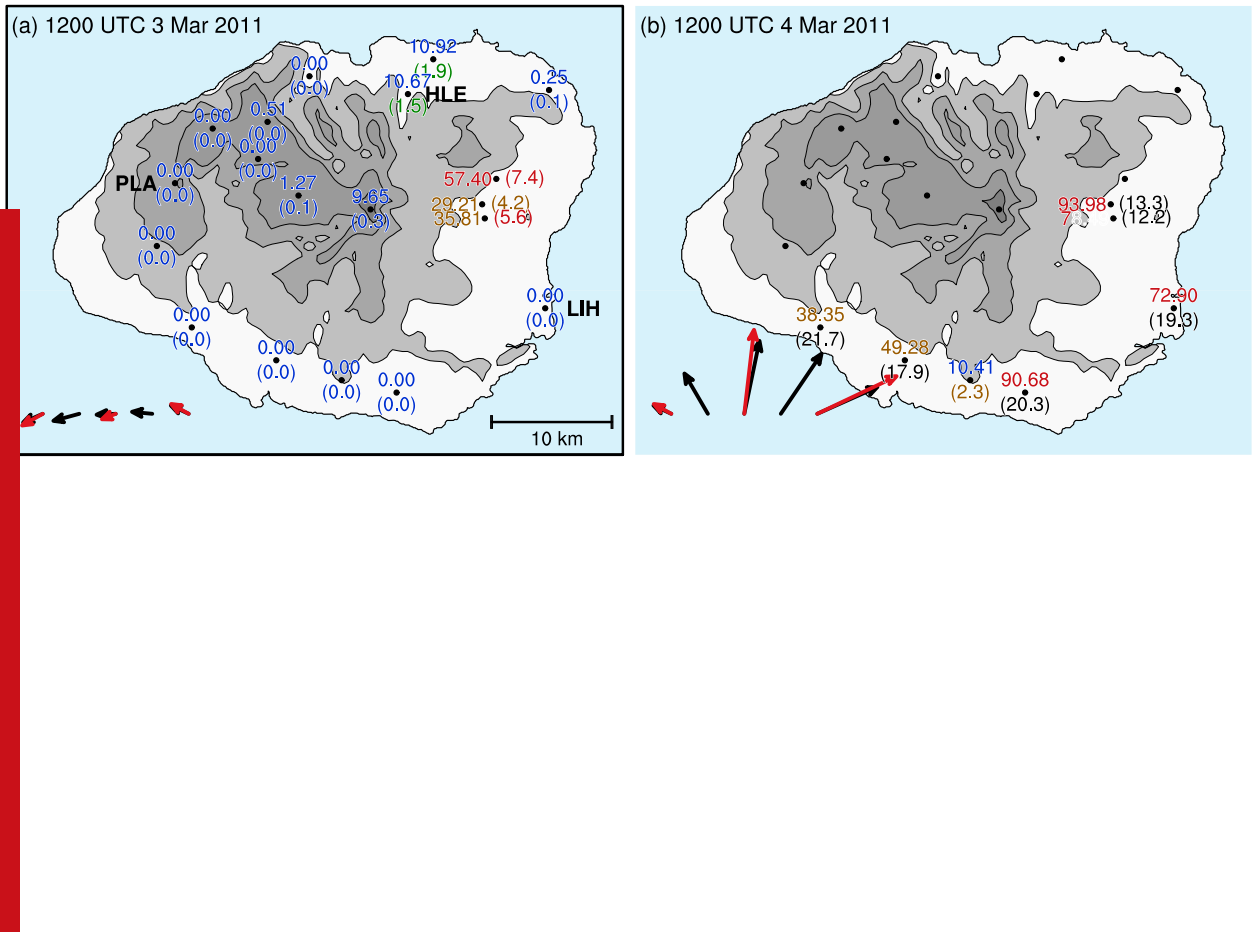

ayer to be realized (Fig. 16d) via orographically forced scent up the 1.5-km-tall terrain.

To further quantify the meteorological conditions mpacting Kauai, we calculated the layer-mean IVT etween 1000 and 850 hPa (i.e., below the island's ighest terrain) from the twice-daily soundings at LIH nd from the 6-h-resolution CFSR output using an av-rage of the six grid points closest to the island (bounded y 22.0°–22.5°N, 159.0°–160.0°W). The observations and FSR yielded qualitatively similar results (Fig. 14). For he 24-h period ending 1200 UTC 3 March (Fig. 14a), weak westward-directed (i.e., trade wind) water vapor fluxes impacted Kauai, resulting in modest rainfall on the east side of the island. During the follow-on 24-h period ending 1200 UTC 4 March (Fig. 14b), the water vapor transport vector strengthened markedly while rotating to southerly and then southwesterly within the AR. Consequently, very heavy orographic rains fell on the normally dry southern and western side of the island, although significant rainfall was observed island-wide due to the deep-layer moisture, ascent, and weak stability with the AR. Between 1200 UTC 4 March and 1200 UTC

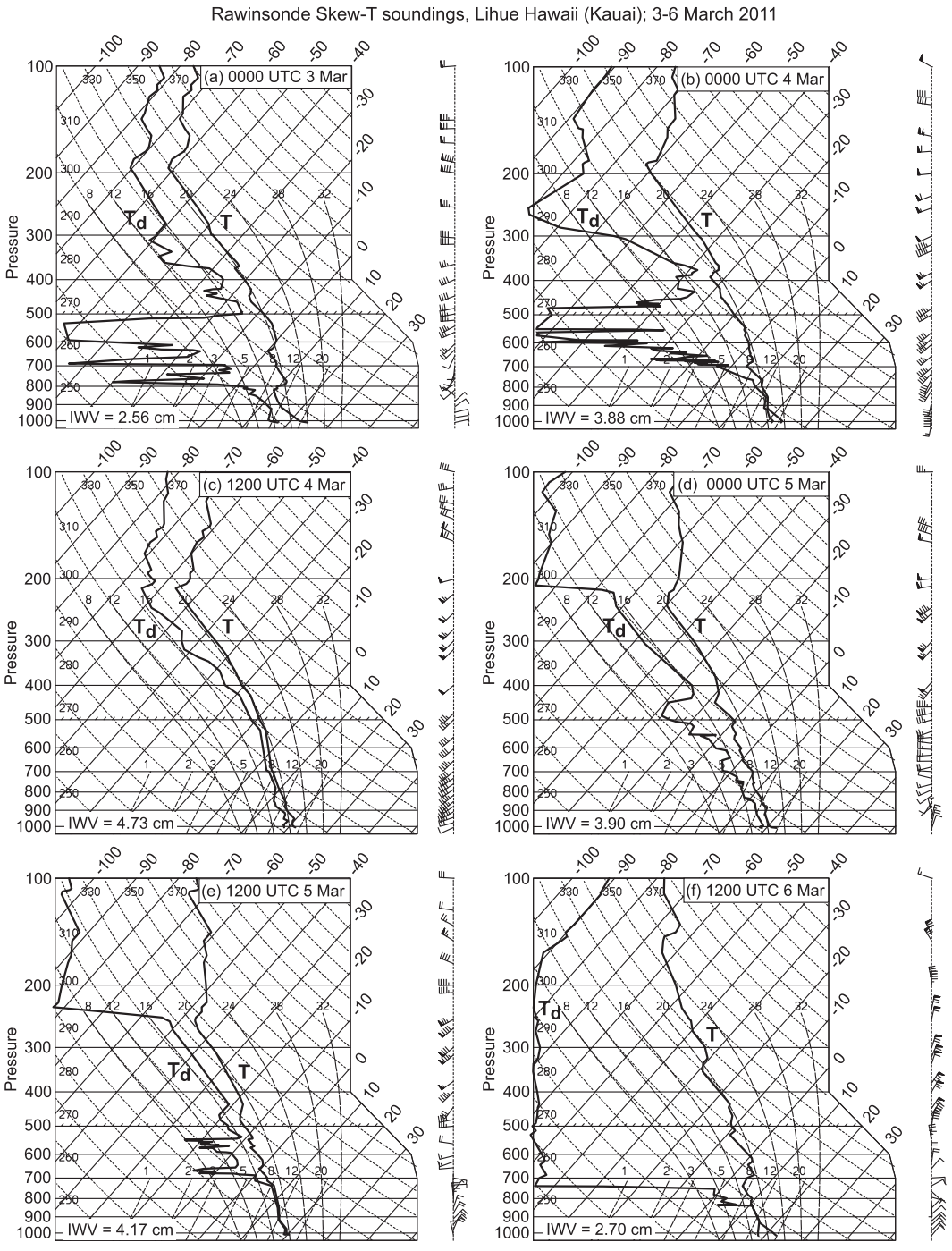

FIG. 15. Skew T–log$p$ diagrams of rawinsonde soundings from Lihue, HI, at (a) 0000 UTC 3 Mar, (b) 0000 UTC 4 Mar, (c) 1200 UTC 4 Mar, (d) 0000 UTC 5 Mar, (e) 1200 UTC 5 Mar, and (f) 1200 UTC 6 Mar 2011. Profiles of temperature (T) and dewpoint temperature (T_d) are labeled, and IWV values (cm) are given. Wind flags and barbs are as in Fig. 3.

5 March (Fig. 14c), the shallow frontal passage shifted the IVT vector back to a more typical southwestward-directed pattern. Heavy rains continued due to the combined effects of orography and the AR. During the final 24-h period ending 1200 UTC 6 March (Fig. 14d), moderate intensity IVT persisted from the northeast, yielding a more typical windward rainfall maximum.

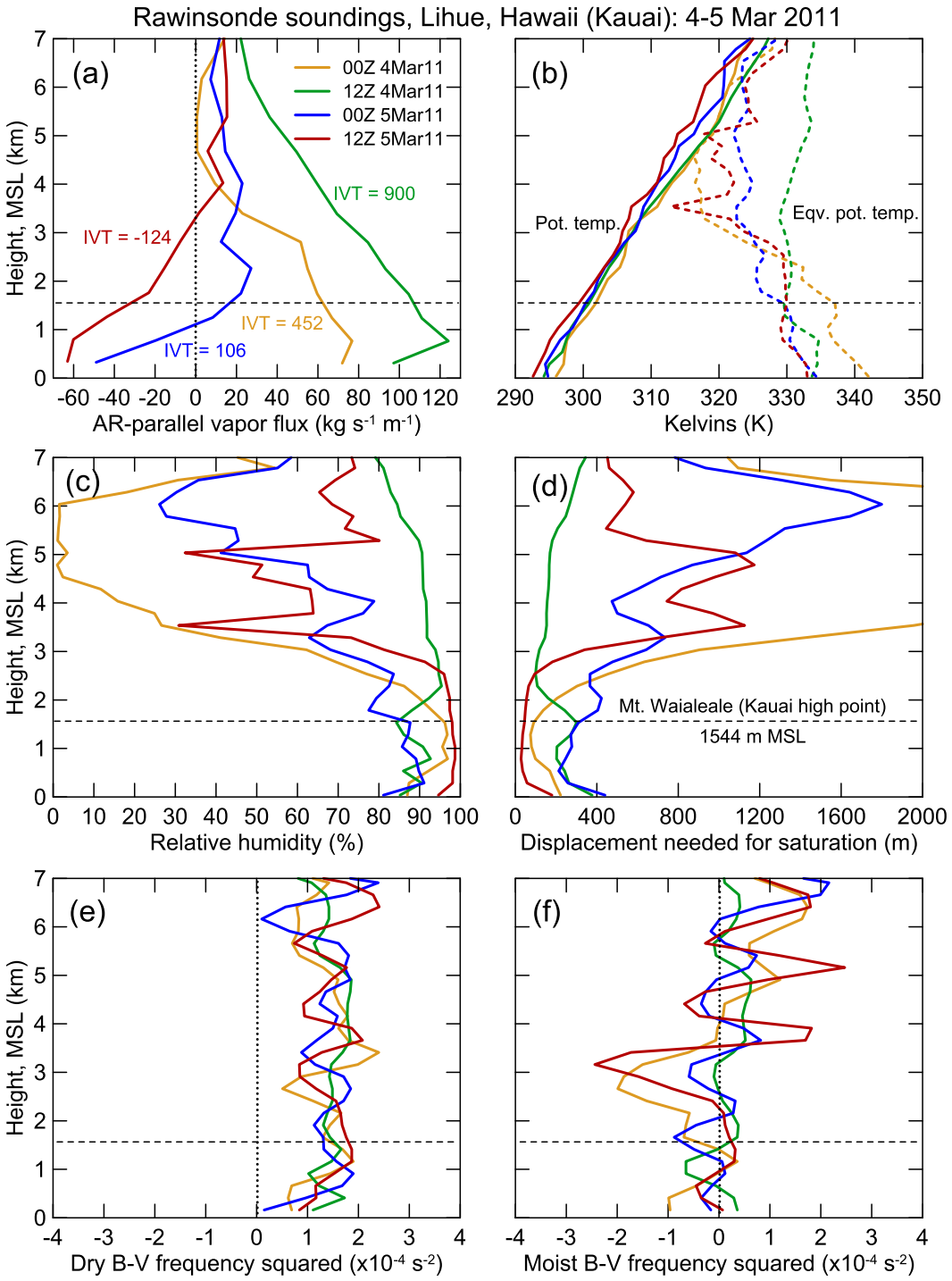

FIG. 16. Profiles from the Lihue, HI, rawinsonde soundings at 0000 UTC 4 Mar, 1200 UTC 4 Mar, 0000 UTC 5 Mar, and 1200 UTC 5 Mar 2011 (color coded, see legend): (a) AR-parallel horizontal water vapor flux ($kg\,s^{-1}\,m^{-1}$; directed from 235°); (b) θ (K; solid) and θ_e (K; dashed); (c) relative humidity (%); (d) vertical displacement (m) required for saturation; (e) square of the dry Brunt–Väisälä frequency ($\times 10^{-4}\,s^{-2}$); and (f) square of the moist Brunt–Väisälä frequency ($\times 10^{-4}\,s^{-2}$). The 1000–200-hPa AR-parallel IVT magnitudes ($kg\,s^{-1}\,m^{-1}$) are shown next to their companion profiles in (a). The altitude of Kauai's high point (Mt. Waialeale—1544 m MSL) is marked on each panel with a horizontal dashed line. The vertical dotted line in (a),(e), and (f) marks the 0 value.

The rawinsonde observations (Figs. 15–16), together with the G-IV dropsonde analyses over the nearby open ocean (Figs. 10–13) and the low-level IVT diagnostics (Fig. 14), help explain the heavy rainfall on Kauai. The erosion of the trade wind inversion by large-scale lift aloft with the advancing AR and upper cold front resulted in deep-layer clouds and rainfall island wide. Potential instability in this deep moist environment was released via orographic uplift, resulting in abnormally heavy rains in orographically favored regions, including on the normally dry southwest side of the island where upslope southwesterly flow occurred on the equatorward side of the AR. The high Puu Lua site at 1021 m MSL on the west side of Kauai (PLA in Fig. 14a) recorded a southwesterly wind direction in AR conditions between 0100 and 2000 UTC 4 March (not shown), during which 106 mm of rain fell (i.e., 72% of the rainfall during the 96-h period in Fig. 14). This represents 71% of their March monthly rainfall average in only 19 h. Consistent northeasterly trade winds were observed on either side of this time window. On the normally wet northeast side of Kauai, the Hanalei River gauge (HLE in Fig. 14a) provided representative observations of the anomalous runoff caused by the heavy rains. The HLE gauge recorded peak flows of 192 and 178 $m^3 s^{-1}$ at 0720 UTC 4 March and 0125 UTC 5 March 2011 (not shown), which were among the largest flows observed during water year 2011 and much larger than the ~4$m^3 s^{-1}$ median climatological flow expected for early March.

6. Conclusions

The Winter Storms and Pacific Atmospheric Rivers (WISPAR) experiment was carried out between January and March 2011 at NASA's DFRC in California to serve as a demonstration test bed for utilizing unmanned aerial systems with dropsondes in meteorological research and operations over data-sparse oceanic regions. One of three unmanned Global Hawk flights was coordinated with a NOAA G-IV Winter Storms Reconnaissance Program flight out of Honolulu, Hawaii, on 3–4 March 2011. The G-IV, which flew through a developing AR west of Hawaii on those days, represents the cornerstone observing platform for this study. The flight provided the southernmost airborne observations of an AR published to date in the subtropical Northern Hemisphere.

NOAA/NCEP's CFSR and GDAS global gridded datasets and the HYSPLIT trajectory tool provided synoptic-scale context for the AR analyzed in this study. Plan-view analyses show the AR developed west of Hawaii over a region of substantial upward sea surface latent heat fluxes and within a transient southern branch shortwave trough that exported water vapor poleward from the tropics. The trough and associated AR ultimately became entrained into the midlatitude circulation and subsequently weakened in an environment lacking significant upward sea surface latent heat fluxes and dynamical forcing as they approached the U.S. West Coast. Back-trajectories ending in the developing AR west of Hawaii possessed air parcel origins from points south in the moist tropics, whereas most trajectories terminating north of the AR originated in the drier midlatitudes. Companion forward trajectories beginning in the developing AR raced northeastward toward the U.S. West Coast and ascended into the upper troposphere, such that the airstream was depleted of water vapor upon reaching the continent. North of the developing AR, the forward trajectories starting at low levels moved primarily equatorward in a moist airstream while their upper-level counterparts drifted slowly southeastward.

Airborne dropsonde observations from the NASA G-IV aircraft afforded a plan-view and cross-section mesoscale depiction of the structural characteristics in the subtropical AR west of the Hawaii. The AR exhibited characteristics comparable to those observed previously farther north in the subtropics and midlatitudes (e.g., Ralph et al. 2004, 2005, 2011; Neiman et al. 2008a, 2008b, 2011, 2013), save for larger IWV and weaker winds in the AR core and the strong equatorward vapor fluxes in the shallow post-cold-frontal northeasterly flow. A set of eight dropsondes released in a ~200-km-wide box formation provided a first-of-its-kind kinematic assessment of tropospheric vorticity, divergence (mass, water vapor, and sensible heat), and vertical velocity in the AR region, as well as sea surface fluxes from the ocean surface. The budget-box diagnostics were physically consistent with the larger-scale meteorological analyses based on the global gridded reanalysis datasets, while they also provided useful additional, finer-scale kinematic information described above. The dropsonde analyses and diagnostics also offer a framework for future AR-related research and operational uses of high-altitude, long-range reconnaissance aircraft, such as NASA's Global Hawk, which was the focus of the WISPAR field campaign. It should be noted that the budget box was positioned across the low-level cold-frontal shear zone on the poleward edge of the AR rather than within the core of the AR. Future dropsonde budget-box deployments should also strive to target the core region of ARs.

This paper is the first to our knowledge that explores AR influences on rainfall in Hawaii. The AR studied here produced heavy orographically enhanced rainfall and flooding across the state's rugged terrain, especially on the island of Kauai. Significantly, the normally dry southwestern side of Kauai also received heavy rain as

the moist, low-level, potentially unstable southwesterly airstream in the core of the AR ascended the steep terrain there. Based on this case study, it is plausible to hypothesize that ARs contribute significantly to the annual rainfall totals on the normally dry sides of the islands and on the high summits of Maui and the Big Island, although a climatologically based composite analysis would be required to prove or refute this assertion. The precipitation falling across the West Coast states with this AR was also modulated by steep orography, but the impacts were modest by comparison. These results suggest that the early evolution of an AR originating in the tropics does not necessarily determine how the AR will evolve later as it extends into midlatitudes. Rather, the maintenance of a strong AR emerging from the tropics likely relies on the presence of consistent midlatitude dynamical support (e.g., low-level convergence, frontogenesis) as described in Cordeira et al. (2013).

Acknowledgments. We thank Robbie Hood (NOAA/UAS Program Manager) for providing the resources to carry out the WISPAR field campaign. Yucheng Song and Bill Lapenta (NOAA/NCEP Environmental Modeling Center) graciously enabled the Winter Storms Program NOAA G-IV to participate in WISPAR. Kevin Kodama at the NWS WFO in Honolulu provided observational data in Hawaii. Jim Adams and Allen White assisted in the generation of graphics. We are grateful for the comments and suggestions offered by Janet Intrieri of NOAA, Kelly Mahoney and Mimi Hughes of CIRES, Jason Cordeira of Plymouth State University, and an anonymous reviewer. Their efforts improved the scope and quality of this manuscript.

REFERENCES

Albrecht, B. A., 1984: A model study of downstream variations of the thermodynamic structure of the trade winds. *Tellus,* **36A,** 187–202, doi:10.1111/j.1600-0870.1984.tb00238.x.

Bao, J.-W., S. A. Michelson, P. J. Neiman, F. M. Ralph, and J. M. Wilczak, 2006: Interpretation of enhanced integrated water vapor bands associated with extratropical cyclones: Their formation and connection to tropical moisture. *Mon. Wea. Rev.,* **134,** 1063–1080, doi:10.1175/MWR3123.1.

Berg, W., and R. Chase, 1992: Determination of mean rainfall from the Special Sensor Microwave/Imager (SSM/I) using a mixed lognormal distribution. *J. Atmos. Oceanic Technol.,* **9,** 129–141, doi:10.1175/1520-0426(1992)009<0129:DOMRFT>2.0.CO;2.

Cao, G., T. W. Giambelluca, D. E. Stevens, and T. A. Schroeder, 2007: Inversion variability in the Hawaiian trade wind regime. *J. Climate,* **20,** 1145–1160, doi:10.1175/JCLI4033.1.

Cordeira, J. M., F. M. Ralph, and B. J. Moore, 2013: The development and evolution of two atmospheric rivers in proximity to western North Pacific tropical cyclones in October 2010. *Mon. Wea. Rev.,* **141,** 4234–4255, doi:10.1175/MWR-D-13-00019.1.

Dee, D., and Coauthors, 2011: The ERA-Interim reanalysis: Configuration and performance of the data assimilation system. *Quart. J. Roy. Meteor. Soc.,* **137,** 553–597, doi:10.1002/qj.828.

Dettinger, M. D., F. M. Ralph, T. Das, P. J. Neiman, and D. Cayan, 2011: Atmospheric rivers, floods, and the water resources of California. *Water,* **3,** 445–478, doi:10.3390/w3020445.

Draxler, R. R., and G. D. Hess, 1997: Description of the HYSPLIT_4 modeling system. NOAA Tech. Memo. ERL-ARL-224, NOAA/Air Resources Laboratory, Silver Spring, MD, 24 pp.

——, and G. D. Rolph, cited 2011: HYSPLIT (HYbrid Single-Particle Lagrangian Integrated Trajectory) model. NOAA/Air Resources Laboratory, Silver Spring, MD. [Available online at http://ready.arl.noaa.gov/HYSPLIT.php.]

Fairall, C. W., E. F. Bradley, J. E. Hare, A. A. Grachev, and J. B. Edson, 2003: Bulk parameterization of air–sea fluxes: Updates and verification for the COARE algorithm. *J. Climate,* **16,** 571–591, doi:10.1175/1520-0442(2003)016<0571:BPOASF>2.0.CO;2.

Fujita, T. T., 1963: Analytical mesometeorology: A review. *Severe Local Storms, Meteor. Monogr.,* No. 27, Amer. Meteor., Soc., 77–125.

Garreaud, R., 2013: Warm winter storms in central Chile. *J. Hydrometeor.,* **14,** 1515–1534, doi:10.1175/JHM-D-12-0135.1.

Giambelluca, T. W., Q. Chen, A. G. Frazier, J. P. Price, Y.-L. Chen, P.-S. Chu, J. K. Eischeid, and D. M. Delparte, 2013: Online rainfall atlas of Hawai'i. *Bull. Amer. Meteor. Soc.,* **94,** 313–316, doi:10.1175/BAMS-D-11-00228.1.

Guan, B., N. P. Molotch, D. E. Waliser, E. J. Fetzer, and P. J. Neiman, 2010: Extreme snowfall events linked to atmospheric rivers and surface air temperature via satellite measurements. *Geophys. Res. Lett.,* **37,** L20401, doi:10.1029/2010GL044696.

——, ——, ——, ——, and ——, 2013: The 2010/11 snow season in California's Sierra Nevada: Role of atmospheric rivers and modes of large-scale variability. *Water Resour. Res.,* **49,** 6731–6743, doi:10.1002/wrcr.20537.

Kalnay, E., and Coauthors, 1996: The NCEP/NCAR 40-Year Reanalysis Project. *Bull. Amer. Meteor. Soc.,* **77,** 437–471, doi:10.1175/1520-0477(1996)077<0437:TNYRP>2.0.CO;2.

Karstens, U., C. Simmer, and E. Ruprect, 1994: Remote sensing of cloud liquid water. *Meteor. Atmos. Phys.,* **54,** 157–171, doi:10.1007/BF01030057.

Knippertz, P., and J. E. Martin, 2005: Tropical plumes and extreme precipitation in subtropical and tropical West Africa. *Quart. J. Roy. Meteor. Soc.,* **131,** 2337–2365, doi:10.1256/qj.04.148.

Kunkee, D., G. A. Poe, D. Boucher, S. Swadley, Y. Hong, J. Wessel, and E. Uliana, 2008: Design and evaluation of the first Special Sensor Microwave Imager/Sounder (SSMIS). *IEEE Trans. Geosci. Remote Sens.,* **46,** 863–883, doi:10.1109/TGRS.2008.917980.

Lavers, D. A., and G. Villarini, 2013: The nexus between atmospheric rivers and extreme precipitation across Europe. *Geophys. Res. Lett.,* **40,** 3259–3264, doi:10.1002/grl.50636.

——, R. P. Allan, E. F. Wood, G. Villarini, D. J. Brayshaw, and A. J. Wade, 2011: Winter floods in Britain are connected to atmospheric rivers. *Geophys. Res. Lett.,* **38,** L23803, doi:10.1029/2011GL049783.

McBride, J. L., B. W. Gunn, G. J. Holland, T. D. Keenan, and N. E. Davidson, 1989: Time series of total heating and moistening over the Gulf of Carpentaria radiosonde array during AMEX. *Mon. Wea. Rev.,* **117,** 2701–2713, doi:10.1175/1520-0493(1989)117<2701:TSOTHA>2.0.CO;2.

Moore, G. J., P. J. Neiman, F. M. Ralph, and F. Barthold, 2012: Physical processes associated with heavy flooding rainfall in

Nashville, Tennessee, and vicinity during 1–2 May 2010: The role of an atmospheric river and mesoscale convective systems. *Mon. Wea. Rev.,* **140,** 358–378, doi:10.1175/MWR-D-11-00126.1.

Neiman, P. J., F. M. Ralph, G. A. Wick, J. Lundquist, and M. D. Dettinger, 2008a: Meteorological characteristics and overland precipitation impacts of atmospheric rivers affecting the west coast of North America based on eight years of SSM/I satellite observations. *J. Hydrometeor.,* **9,** 22–47, doi:10.1175/2007JHM855.1.

——, ——, ——, Y.-H. Kuo, T.-K. Wee, Z. Ma, G. H. Taylor, and M. D. Dettinger, 2008b: Diagnosis of an intense atmospheric river impacting the Pacific Northwest: Storm summary and offshore vertical structure observed with COSMIC satellite retrievals. *Mon. Wea. Rev.,* **136,** 4398–4420, doi:10.1175/2008MWR2550.1.

——, L. J. Schick, F. M. Ralph, M. Hughes, and G. A. Wick, 2011: Flooding in western Washington: The connection to atmospheric rivers. *J. Hydrometeor.,* **12,** 1337–1358, doi:10.1175/2011JHM1358.1.

——, F. M. Ralph, B. J. Moore, M. Hughes, K. M. Mahoney, J. Cordeira, and M. D. Dettinger, 2013: The landfall and inland penetration of a flood-producing atmospheric river in Arizona. Part I: Observed synoptic-scale, orographic, and hydrometeorological characteristics. *J. Hydrometeor.,* **14,** 460–484, doi:10.1175/JHM-D-12-0101.1.

Otkin, J. A., and J. E. Martin, 2004: A synoptic climatology of the subtropical kona storm. *Mon. Wea. Rev.,* **132,** 1502–1517, doi:10.1175/1520-0493(2004)132<1502:ASCOTS>2.0.CO;2.

Ralph, F. M., P. J. Neiman, and G. A. Wick, 2004: Satellite and CALJET aircraft observations of atmospheric rivers over the eastern North Pacific Ocean during the winter of 1997/98. *Mon. Wea. Rev.,* **132,** 1721–1745, doi:10.1175/1520-0493(2004)132<1721:SACAOO>2.0.CO;2.

——, ——, and R. Rotunno, 2005: Dropsonde observations in low-level jets over the northeastern Pacific Ocean from CALJET-1998 and PACJET-2001: Mean vertical-profile and atmospheric-river characteristics. *Mon. Wea. Rev.,* **133,** 889–910, doi:10.1175/MWR2896.1.

——, ——, G. A. Wick, S. I. Gutman, M. D. Dettinger, D. R. Cayan, and A. B. White, 2006: Flooding on California's Russian River: The role of atmospheric rivers. *Geophys. Res. Lett.,* **33,** L13801, doi:10.1029/2006GL026689.

——, ——, G. N. Kiladis, K. Weickmann, and D. M. Reynolds, 2011: A multiscale observational case study of a Pacific atmospheric river exhibiting tropical–extratropical connections and a mesoscale frontal wave. *Mon. Wea. Rev.,* **139,** 1169–1189, doi:10.1175/2010MWR3596.1.

Reynolds, R. W., T. M. Smith, C. Liu, D. B. Chelton, K. S. Casey, and M. G. Schlax, 2007: Daily high-resolution blended analyses for sea surface temperature. *J. Climate,* **20,** 5473–5496, doi:10.1175/2007JCLI1824.1.

Riehl, H., 1979: *Climate and Weather in the Tropics.* Academic Press, 623 pp.

Rienecker, M. M., and Coauthors, 2011: MERRA: NASA's Modern-Era Retrospective Analysis for Research and Applications. *J. Climate,* **24,** 3624–3648, doi:10.1175/JCLI-D-11-00015.1.

Saha, S., and Coauthors, 2010: The NCEP Climate Forecast System Reanalysis. *Bull. Amer. Meteor. Soc.,* **91,** 1015–1057, doi:10.1175/2010BAMS3001.1.

Saucier, W. J., 1955: *Principles of Meteorological Analysis.* Dover Publications, 438 pp.

Schroeder, T. A., 1993: Climate controls. *Prevailing Trade Winds: Weather and Climate in Hawai'i,* M. Sanderson, Ed., University of Hawaii Press, 12–36.

Simpson, R. H., 1952: Evolution of the kona storm, a subtropical cyclone. *J. Meteor.,* **9,** 24–35, doi:10.1175/1520-0469(1952)009<0024:EOTKSA>2.0.CO;2.

Sodemann, H., and A. Stohl, 2013: Moisture origin and meridional transport in atmospheric rivers and their association with multiple cyclones. *Mon. Wea. Rev.,* **141,** 2850–2868, doi:10.1175/MWR-D-12-00256.1.

Stohl, A., C. Forster, and H. Sodemann, 2008: Remote sources of water vapor forming precipitation on the Norwegian west coast at 60°N—A tale of hurricanes and an atmospheric river. *J. Geophys. Res.*, **113,** D05102, doi:10.1029/2007JD009006.

Szunyogh, I., Z. Toth, A. V. Zimin, S. J. Majumdar, and A. Persson, 2002: Propagation of the effect of targeted observations: The 2000 Winter Storm Reconnaissance Program. *Mon. Wea. Rev.,* **130,** 1144–1165, doi:10.1175/1520-0493(2002)130<1144:POTEOT>2.0.CO;2.

Taylor, G. I., 1938: The spectrum of turbulence. *Proc. Roy. Soc. London,* **164A,** 476–490, doi:10.1098/rspa.1938.0032.

Viale, M., and M. N. Nuñez, 2011: Climatology of winter orographic precipitation over the subtropical central Andes and associated synoptic and regional characteristics. *J. Hydrometeor.,* **12,** 481–507, doi:10.1175/2010JHM1284.1.

Wentz, F. J., 1995: The intercomparison of 53 SSM/I water vapor algorithms. Tech. Rep., Remote Sensing Systems, Santa Rosa, CA, 19 pp.

Zhu, Y., and R. E. Newell, 1994: Atmospheric rivers and bombs. *Geophys. Res. Lett.,* **21,** 1999–2002, doi:10.1029/94GL01710.

——, and ——, 1998: A proposed algorithm for moisture fluxes from atmospheric rivers. *Mon. Wea. Rev.,* **126,** 725–735, doi:10.1175/1520-0493(1998)126<0725:APAFMF>2.0.CO;2.